International Journal of Fatigue 208 (2026) 109566

Contents lists available at ScienceDirect

International Journal of Fatigue

journal homepage: www.elsevier.com/locate/ijfatigue

Fatigue and fracture properties of Al2618 + TiB_2-reinforced metal matrix composite produced by Laser-powder bed fusion☆

Luca Mariotti [a], Giorgia Lupi [a], Alessio Pozzoli [a], Stefano Beretta [a,d], Bartosz Madejski [b], Donato Girolamo [c], Riccardo Casati [a], Luca Patriarca [a,*]

[a] Department of Mechanical Engineering, Politecnico di Milano, Via G. La Masa 34, 20156 Milano (MI), Italy
[b] Łukasiewicz Research Network – Institute of Aviation, al. Krakowska 110/114, 02-256 Warsaw, Poland
[c] European Space Agency, Keplerlaan 1, 2201 AZ Noordwijk, the Netherlands
[d] Auburn University, National Center for Additive Manufacturing Excellence (NCAME), Auburn, Al 36849, USA

ARTICLE INFO

Keywords:
Metal Matrix Composite
Fracture Properties
Defects Analysis
Mechanical Characterization
Powder Bed Fusion
Powder Functionalization
Fatigue Properties

ABSTRACT

Metal Matrix Composites (MMCs) represent a class of materials where a reinforcement phase is added to a metallic alloy to enhance specific functional and mechanical properties. Initially developed for aerospace applications in the mid-twentieth century, MMCs have recently received renewed interest thanks to the possibility of being processed by additive manufacturing processes. This study aims to investigate the fatigue and fracture properties of the Al2618 alloy reinforced by 7.1 wt% TiB_2 particles, produced via the Powder Bed Fusion Laser Beam (PBF-LB) process. The original gas-atomized Al2618 powder was initially pre-alloyed by 1.30 wt% of TiB_2; successively, the target 7.10 wt% TiB_2 content was achieved by high-energy mechanical mixing with additional TiB_2 powder. The resulting MMC exhibited increased elastic modulus and tensile strength compared to the unreinforced Al2618 alloy.

In the second part of the study, a comprehensive characterization of the fatigue and fracture properties was carried out, further demonstrating the promising structural properties of the present MMC. Fracture toughness (KIC) tests were performed with the crack plane along three different orientations. Fatigue crack growth properties were instead assessed in the primary vertical orientation; these data were used to interpret the fatigue experiments conducted on net-shape specimens. Detailed fracture surface analyses, supported by computed tomography scans, enabled extensive characterization of the defects generated in this MMC pointing to the complexity of manufacturing this material. Overall, this work provides a comprehensive characterization of the structural performance of Al-based MMCs produced by PBF-LB, establishing a reference framework for researcher and industry to approach damage-tolerance-based assessment on this class of materials.

1. Introduction

Additive Manufacturing (AM) of metallic alloys has experienced rapid growth over the past decade, offering the capability to produce geometrically complex components that are difficult, or even impossible, to achieve through conventional manufacturing methods. Among the various AM techniques, Powder Bed Fusion using a Laser Beam (PBF-LB) has emerged as one of the most widely adopted processes across multiple industrial sectors [1,2]. PBF-LB technique has recently reached a technology maturity which guarantees the industrial production of structural components with high printing quality, and it is therefore expected to be further adopted for large-scale productions.

Currently, research efforts are directed toward the design and optimization of metallic alloys specifically tailored for the AM process [3]. These alloys combine superior physical and mechanical properties, including high strength, low weight, and elevated thermal conductivity, together with high AM processability, and are designed to meet the stringent requirements of advanced applications, particularly in the aerospace sector [4–9]. A complementary strategy for further improving functional and mechanical properties involves the use of metal matrix composites (MMCs) which have recently emerged as promising alloys for AM applications. MMCs consists of a metal matrix reinforced with a

☆ This article is part of a special issue entitled: 'FDMD 5' published in International Journal of Fatigue.

* Corresponding author.
E-mail address: luca.patriarca@polimi.it (L. Patriarca).

https://doi.org/10.1016/j.ijfatigue.2026.109566
Received 7 November 2025; Received in revised form 16 January 2026; Accepted 10 February 2026
Available online 12 February 2026

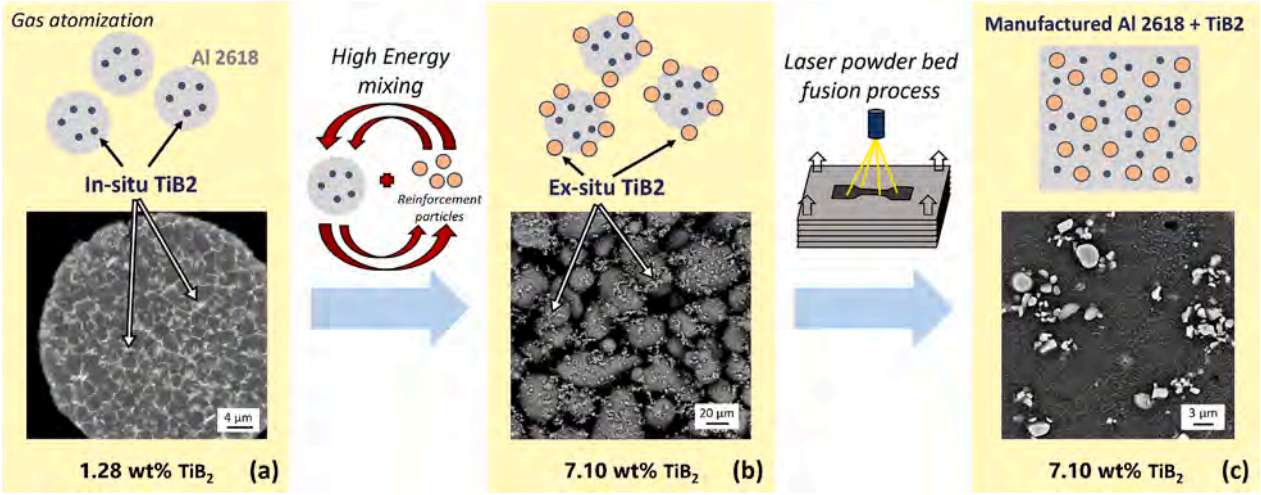

Fig. 1. Powder feedstock production sequence with wt% of TiB_2 [20] and final composite microstructure after manufacturing.

fraction of specific reinforcement with higher mechanical properties (i.e. elastic modulus, strength, etc). MMCs for AM process can be obtained by adding micro- or nano- sized ceramic particles (such as borides, carbides, oxides, nitrides or a combination of those) into a metallic matrix [10–15]. Among all the MMCs, Aluminium-based Matrix Composites are generating a large interest especially for the excellent mechanical, lightweight and wear properties [16].

MMCs can be produced through a variety of techniques, such as powder metallurgy, friction stir processing, induction melting, and cold spray deposition [17,18]. However, the fabrication of MMCs using conventional technologies presents several challenges. Firstly, these materials require complex manufacturing processes to achieve a homogeneous dispersion of the reinforcement particles. Moreover, the presence of hard and abrasive ceramic reinforcements makes conventional machining difficult. As it will be shown in the present paper, one possibility to overcome these limitations is given by the AM technologies [19], specifically the PBF-LB process. Successful PBF-LB processing of MMCs requires careful preparation of the feedstock powder. In a previous investigation, the authors of the present work developed and compared different techniques for producing Al2618-based feedstock powders incorporating approximately 7 wt% TiB_2 particles [20,21]. Referring to the so-called in-situ approach, ceramic nanoparticles were synthesized through the precipitation of ceramic compounds directly within the molten alloy during atomization or printing, via controlled chemical reactions between alloying elements. However, this method may be unsuitable for powders which require a high fraction of reinforcement [22,23]. Alternatively, the ex-situ approach involves the external synthesis of ceramic particles, which are then mechanically incorporated with the metallic matrix powder. Various techniques are used to attach the ceramic particles to the metal powder, including mechanical methods (blending, milling), electrochemical deposition, and physical approaches (plasma coating) [24]. In the case of ex-situ approach, the powder feedstock preparation is inherently challenging: strong interparticle bonding between metal and ceramic particles is essential to prevent detachment of the reinforcement particles during sieving and powder reuse. Additionally, achieving a homogeneous distribution of the reinforcement in the feedstock powder is crucial, as it directly ensures uniform dispersion in the final printed composite [18].

In the present work, the Al2618 + 7.1 wt% TiB_2 MMC powder was produced leveraging both in-situ and ex-situ approaches. The feedstock produced with this novel technique was successfully used to fabricate standard specimens for material characterization via PBF-LB: tensile, fracture toughness, fatigue crack growth and fatigue samples. Subsequently, a comprehensive static and fatigue characterization of the MMC was carried out to address the gap in the literature, which currently lacks investigations covering a broad range of mechanical and microstructural aspects of MMCs. The resulting material property dataset is crucial for evaluating the potential adoption of the studied MMC in targeted engineering applications and for implementing damage-tolerance-based approaches to design. The study also focuses on the type of defects that are seen to influence and determine the fatigue performances of the manufactured parts. Detailed high-resolution X-ray computed tomography (XCT) scans were performed on the fatigue specimens before testing. The defects maps were generated for bulk, subsurface and surface critical defects providing a unique set of defect populations for interpreting the fatigue failures in this MMC. Finally, a structural assessment based on the damage tolerance approach was demonstrated to be suited for predicting the fatigue life of MMC [25–27].

The paper is structured as follows. Section 2 (Materials and methods) outlines the novel approach developed to produce the initial powder feedstock and details the experimental procedures adopted for microstructural and mechanical characterization. Section 3 (Results and Discussion) presents the experimental outcomes of tensile, fracture toughness, fatigue crack propagation and fatigue tests. The same section also reports the XCT analyses, providing a quantitative description of the location, shape and size of critical defects. The results are discussed and compared with data available in literature for other additively manufactured (AMed) MMCs and conventional aerospace Al alloys. Particular emphasis is placed on assessing the competitiveness of the investigated AMed-MMC relative to alloys such as Scalmalloy® and AlSi10Mg, specifically regarding improvements in stiffness and structural performance. This section also addresses the main challenges related to the processability of this MMC.

2. Materials and methods

2.1. Powder feedstock production

The complete production sequence of the feedstock powder is described in Fig. 1. This process was selected and optimised in a previous work after a comparison among four different feedstock production techniques based on the static mechanical properties of thin-walled specimens [20]. The study shown that the pre-alloying by gas atomization (in-situ technique) is particularly promising for the static properties. However, the resulting TiB_2 content remained limited (2.6 wt%). Higher weight fractions of TiB_2 reinforcement were obtained by high-energy mechanical mixing the Al2618 powder and the TiB_2 powder. For the material in the present study, we combined the two procedures, reaching the final TiB_2 content of 7.1 wt%. The final microstructure exhibits both micro- and nano-sized TiB_2 particles resulting in different

Table 1
Chemical composition and properties of the pre-alloyed Al2618 powder (wt%) provided by the manufacturer.

Chemical composition [%]								
Cu	**Fe**	**Mg**	**Ni**	**Si**	**Ti**	**Zn**	**B**	**Al**
2.5	1.2	1.8	1.2	0.2	2.1	0.01	0.4	Balance
Powder properties								
Particle size D10 (ISO 13320)							28.6 μm	
Particle size D50 (ISO 13320)							43.3 μm	
Particle size D90 (ISO 13320)							66.0 μm	

powder chemical composition and ceramic reinforcement content compared to the previous work [20].

More in detail, the pre-alloyed Al2618 powder was produced by means of the gas atomization process, and its properties are reported in Table 1. The presence of 2.1 wt% of Ti and the 0.4 wt% of B promoted the formation of approximately 1.3 wt% of in-situ TiB_2 particles. These particles are visible in the SEM image of the cross-section of a powder particle in the first step in Fig. 1.a. The pre-alloyed powder was successively mixed with 5.7 wt% of ex-situ TiB_2 particles [28] through a high-energy mechanical mixing process. The TiB_2 particles, characterized by an average diameter of 2 μm, were produced by Treibacher Industrie AG [29]. These TiB_2 particles adhered to the pre-alloyed powder, as shown in the SEM image in Fig. 1.b. The mixing was effective, and it resulted in a uniform dispersion of the ceramic particles with a total ceramic reinforcement content of 7.1 wt% considering both in-situ and ex-situ contributions. The uniformity in the ceramic dispersion is then reflected in the final product after the functionalised powder is AM processed, as shown in the composite final microstructure of Fig. 1.c.

2.2. Specimen production

A dual-laser PBF-LB printer (SLM280, SLM Solutions) was employed to produce the specimens shown in Fig. 2.a, including their quantities and printing orientations. Optimization of the printing parameters was carried out by varying laser power, hatch distance, scan speed, and layer thickness to ensure maximum density of the manufactured specimens. The set of parameters that allowed to achieve the highest material density (99.6%) is summarized in Fig. 2.b.

The geometries of the specimens for mechanical testing are shown in Fig. 2.c. All dimensions were chosen in accordance with the appropriate standard [30–34]. Single Edge Bending (SEB) specimens were selected for fatigue crack growth (FCG) tests to be used on a resonance flexural machine which can ensure high testing frequencies (up to 60 Hz) and thus reduce the testing time especially for the threshold tests. Furthermore, the SEB geometry also enables to cover a large spectrum of load ratios R, both positive and negative ones. Compact Tension (CT) geometry was selected for fracture toughness evaluation. CT geometry allows accessibility to the lateral specimen surface during the test for in-situ Digital Image Correlation (DIC) measurements. In both SEB and CT geometries, the thickness was defined to guarantee a dominant plain strain condition for the crack front. The notches were manufactured using Wire Electrical Discharge Machining (WEDM) to improve geometric tolerances and obtain a narrow notch tip (approximately 200 μm in diameter) which enhances crack nucleation. Axial threaded specimens with 5 mm diameter in the gauge section were designed to perform tensile and fatigue tests. Their lengths, respectively of 84 and 80 mm, were set to the lower limit of the standard to reduce usage of the powder feedstock. For fatigue specimens, a circular cross section of 5 mm in diameter and 19 mm gauge length provides a sufficient volume of material which has statistical relevance for establishing the defect distribution. Fatigue specimens were left in net shape condition with a final sandblasting surface treatment performed using corundum at a pressure of 6 bar. This surface treatment was chosen because it is more representative of the operational conditions of many industrial components produced by PBF-LB. In fact, this treatment is often employed as it can improve the intrinsic limitations of the AM process in terms of surface roughness and surface flaws which can lead to fatigue failure [35].

The vertical orientation with respect to the building plate was selected for the FCG, fatigue, and tensile specimens because it exhibited the poorest tensile performance compared with the D and H orientations in a preliminary phase of the research. Consequently, it represents the lower bound of the material properties and introduces a desirable level of conservatism into the resulting material data package [36]. An exception was made for the CT specimens, for which three orientations were investigated: Vertical (V, 90°), Diagonal (D, 45°) and Horizontal (H, 0°) in order to evaluate the influence of the microstructure on the fracture toughness. All the specimens were subjected to T5 heat treatment (HT), consisting of direct aging at 180 °C for 2 h followed by air cooling. The details related to the HT selection and microstructural analysis are described in a previous work [20].

2.3. Residual stress measurements

In-depth Residual Stresses (RS) were evaluated on one fatigue specimen to assess the stress state following the T5 heat treatment and the sandblasting process. The RS measurement under the surface is a destructive process and a single specimen was therefore used due to the limited total number of fatigue specimens that were preferably

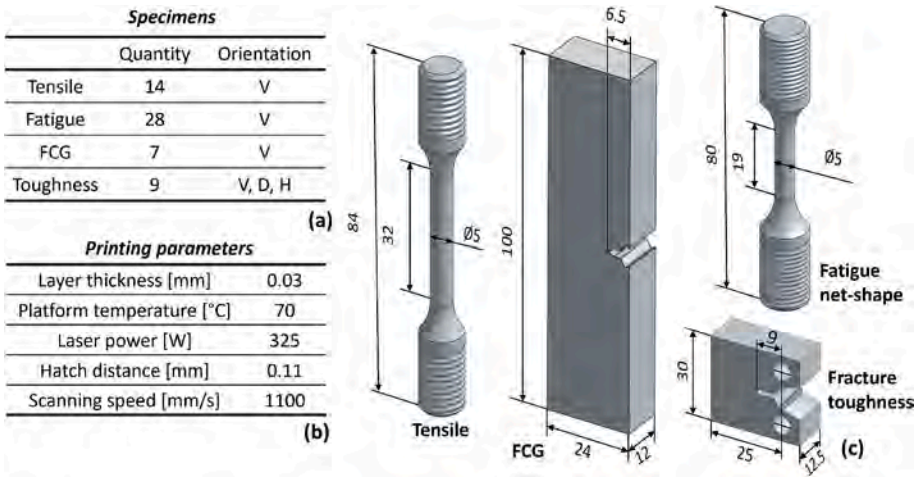

Fig. 2. a) quantity and printing orientation (Vertical, V; Diagonal, D; Horizontal, H) for the printed specimens; b) printing parameters; c) specimens' geometries and most relevant dimensions.

employed in the definition of the SN curve. The RS measurements were taken by means of a X-Stress 3000 AST Stresstech X-ray diffractometer equipped with a 1.5 mm diameter collimator and Cr radiation at 30 kV. The $sin^2\psi$ method was employed using a fixed diffraction angle of $2\theta = 139.3°$. The angular scanning aperture was set to ± 40° with a total of five tilts. RS were performed from the free surface till 400 μm depth with measurements every 50 μm step. Electrolytic polishing carried out using a Struers LectroPol-5 system operating at a voltage of 35 V was used to remove the superficial material. The electrolyte solution consisted of 94% acetic acid (CH3COOH) and 6% perchloric acid (HClO4); polishing times were adjusted for each specimen to achieve the target depth. RS were measured along the directions 0° and 90° with direction 0° aligned with specimen axis and thus with the loading direction. Additional surface measurements (non-destructive) were also taken on other two specimens in directions 0° and 90° to confirm the surface RS data.

2.4. Mechanical testing

2.4.1. Tensile tests

Tensile tests were performed according to the ASTM E8/E8M standard [33] on an MTS Alliance RT100 electro-mechanic tensile machine employing a 25 mm base extensometer. The machine was equipped with a 100 kN load cell and a 2 mm/min displacement rate was applied until complete specimen rupture. Two tensile specimens were dedicated to elastic modulus (E) measurements. An MTS 651 environmental chamber equipped with liquid nitrogen cooling was employed to set the target temperature on the specimen. Each specimen was subjected to ten quasi-static loading and unloading cycles between 10% and 40% of the yield stress with a displacement rate of 1 mm/min. The temperature was varied between −50 °C to + 150 °C with steps of 25 °C. This range was chosen as it is representative of temperatures typically encountered by aluminium components in aerospace applications. For each temperature, E was evaluated with a linear least square fitting on each loading and unloading segment and an average value was calculated.

2.4.2. Fracture toughness tests

Fracture toughness tests on CT were performed according to the ASTM E399 [30] standard under an MTS Landmark RT100 servo-hydraulic machine. Three specimen orientations were investigated: vertical (crack plane parallel to the building direction), diagonal (crack inclined at 45° to the building direction) and horizontal (crack perpendicular to the building direction). The crack opening displacement (COD) was measured using an MTS extensometer with a base of 5 mm. A pre-cracking at load ratio $R = 0.1$ was performed to achieve a 12 mm crack length with a final max stress intensity factor K_{max} of 4.3 MPa $\sqrt{}$ m. A displacement rate of 1 mm/min was applied during the tests until complete specimen failure. Following the tests, images of the fracture surfaces were captured using an optical stereo microscope with 8x magnification lens to measure the final crack length and correct the toughness data. The K_{Isi} (K_I size independent) approach, described in the ASTM standard, was used to obtain a K_I value less sensitive to the size of the specimen.

The microstructure was examined on three CT specimens after testing to further analyse the crack propagation path. The specimens were sectioned transversely to the crack plane, focusing on the central region of the fracture surface, where plane-strain conditions dominate. The samples were mounted in epoxy resin and polished using abrasive papers up to 2400 grit. Final polishing was carried out using 6 μm and 1 μm diamond suspensions before etching with Keller's reagent. Microstructural observations were performed using an optical microscope at 100 × magnification.

2.4.3. Fatigue crack growth tests

Fatigue crack growth tests were conducted on SEB specimens with a resonance flexural Cracktronic Rumul machine which has a maximum mean bending moment of 80 Nm and a maximum bending moment of 160 Nm. A compression pre-cracking (CP) stage was performed in all the specimens at room temperature. The minimum load required for the pre-cracking was chosen employing an elasto-plastic numerical analysis. An amplitude bending moment $Ma = 11.5$ Nm and a mean bending moment Mm = -11.5 Nm were chosen as load that generates an extension of the plastic region at the notch tip of approximately 50 μm. The CP was thus conducted with a minimum equivalent Stress Intensity Factor (SIF) of $K_{min}^{CP} = -3\ MPa\sqrt{m}$ and a maximum of $K_{max}^{CP} = 0\ MPa\sqrt{m}$.

The CP stage helps in obtaining a closure-free crack starting from the EDM notch. More specifically, the tensile RS caused by the compression yielding in the region of the notch leads to a crack nucleation. The crack propagates in the yielded region until the driving force becomes lower than the threshold [37–42]. Compression Pre-cracking Load Reduction (CPLR) tests were performed to evaluate the crack growth threshold ($\Delta K_{th,LC}$) while Compression Pre-cracking Constant Amplitude (CPCA) tests to assess the Paris region of the propagation.

Load ratio $R = 0.7$ was investigated with one CPLR and two CPCA tests to obtain the full Paris-Erdogan curve. $R = 0.7$ is the load ratio commonly referred as the effective one, that is when the crack is fully open and the crack closure mechanisms do not influence the crack propagation rate. Therefore, it can be considered a reference load ratio in the definition of the Paris-Erdogan curve because it represents the upper bound of the crack growth rates [43]. Furthermore, characterizing the $R = 0.7$ is particularly important in our case because the T5 treatment cannot fully mitigate the manufacturing induced tensile residual stresses which can increase the effective R. One CPLR and one CPCA tests were performed at $R = 0$, while for $R = -1$ the priority was given to the threshold values, therefore only two CPLR tests were performed. The crack propagation during the tests was monitored with a 5 mm base Rumul clip-on gauge applied to the specimen notch. Actual initial and final crack lengths were evaluated on the fracture surfaces with the optical stereo microscope. The data processing and crack length correction with actual measurements were completed following prescriptions contained in ASTM E647 [31].

2.4.4. Fatigue testing

Fatigue tests were performed as prescribed in ASTM E466-21 [34] at room temperature with a frequency of 50 Hz and load ratio $R = -1$ for all the specimens. Eight out of twenty-eight specimens were used to estimate the experimental fatigue limit ($\Delta\sigma_w$) with a reduced staircase method as prescribed in the BS ISO 12107:2003 standard [44]. The runout criterion was set at 10^7 cycles and failures were assessed after complete rupture of the specimens. Specimens which reached 10^7 cycles were subsequently retested to analyse the defects at the fracture origins but test results were not used to fit the SN curve.

The line representing the SN curve was obtained by fitting the finite life region of the experimental data with Equation (1), in accordance with ASTM E739 [45]:

$$\boldsymbol{N = A \bullet S^B} \tag{1}$$

The parameters for the data fitting were determined using the maximum likelihood estimation method (MLE) on the logarithmic transformation of Equation (1) as:

$$\boldsymbol{log(N) = log(A) + B \bullet log(S)} \tag{2}$$

Assuming a gaussian distribution for the dependent variable log*(N)* with mean value expressed by Equation (2) and a constant standard deviation σ_{logN} [46]. The scatter on the fatigue limit was calculated from the linear interpolation log*(S)*-log*(N)* line as: $\sigma_{log10(\Delta\sigma w)} = \sigma_{log10(N)} / B$.

A field emission Scanning Electron Microscope (SEM, Zeiss EVO 50XVP Thermionic with the Oxford Inca Energy 200 X-ray microanalysis (EDS) detector) was used to capture images of the fracture surfaces after the fatigue tests. The fractographies were analysed through ImageJ software to properly identify and measure the defects leading to failures.

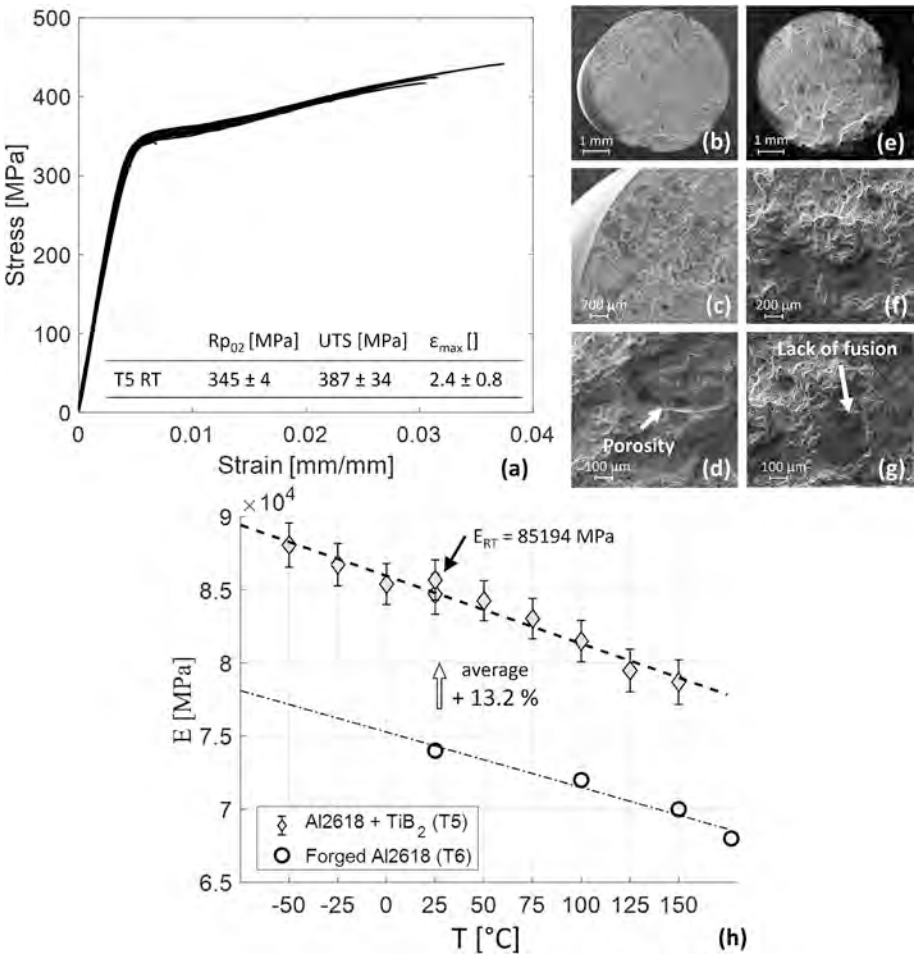

Fig. 3. a) tensile tests results in T5 heat treatment at room temperature; b-g) fracture surfaces at different magnifications; h) elastic modulus variation with temperature compared with literature data on forged Al2618 in T6 heat treatment [49].

In particular, the image processing software was used to measure the area of the killer defects by manually identifying their boundaries and it was also used in measuring the depth of the defects as the distance between the theoretical circular external surface of the specimen and the deepest point of the defect.

2.5. DIC measurements

DIC was employed on three CT specimens to obtain Tresca strain maps on the lateral surface of the specimen at the tip of the crack. The specimens were prepared by spraying white paint and successively black paint to generate a random black and white speckle pattern on a rectangular area. The paints were deposited on the specimen surface using an Iwata CM-B airbrush equipped with a 0.18 mm nozzle diameter. Black spots diameter resulted of approximately 30 ± 4 µm. Blue light at 45° on the sample surface illuminated the specimen to maximize the speckle contrast. The images were captured every 500 ms during the test using a 2 Megapixel Allied Vision Manta CCD optical microscope equipped with a lens system produced by Optem. A field of view of approximately 7.51 × 9.90 mm resulted in a final pixel resolution to 6.1 µm/pixel. The DIC analysis was completed with VIC-2D commercial software while post processing of the strain data was performed through specifically designed Matlab script.

2.6. XCT scan

All the fatigue specimens were scanned with a voxel size of 10 µm. Four scans were carried out for each specimen to obtain a full reconstruction of the entire gauge length. The voltage was set to 70 kV and the current to 150 µA with an integration time of 333 ms. A physical pre-filter consisting of a 0.1 mm copper plate was applied and 1200 projections were acquired. Given the 10 µm voxel size and the segmentation method (triangle), the defect size with a 90% probability of detection results to be 34 µm [47]. This resolution enables an accurate reconstruction of the typical defects in the investigated alloy considering that the minimum defect size from the maxima sampling resulted 90 µm.

3. Results and discussion

This section contains the results in terms of static and fatigue properties obtained in the present study for AM Al2618 + TiB_2 and a comparison with literature data of the base alloy Al2618 produced with conventional manufacturing (forging, casting), along with data on AM aluminium alloys which are commonly employed in advanced applications, especially in the aerospace field, such as Scalmalloy® and AlSi10Mg. The comparison is useful to evaluate the potential adoption of the present alloy for structural applications. The section also contains a discussion on fatigue properties and on the process-induced defects observed on the fracture surfaces and from the XCT data.

3.1. Static properties

See Fig. 3.a shows the tensile stress–strain curves of all the 14 specimens tested. The results demonstrate a good repeatability of the yield condition, providing an average yield strength (Rp_{02}) of 345 MPa with a narrow scatter of 4 MPa. The ultimate load (*UTS*) of 387 MPa and

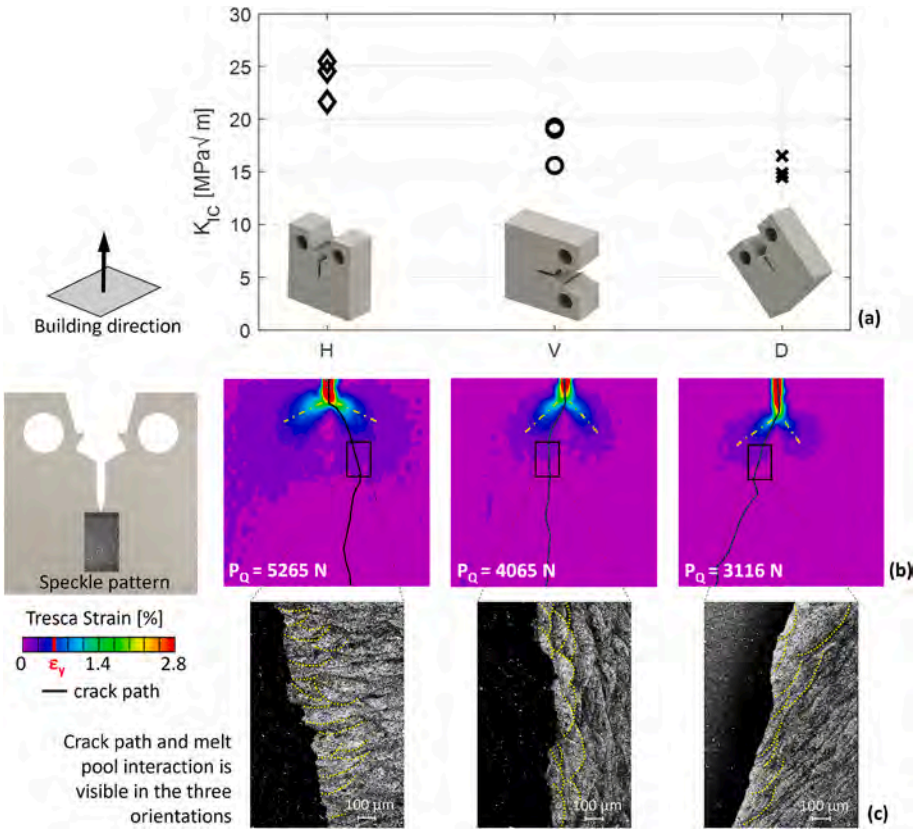

Fig. 4. a) K_{IC} values are reported for the different printing orientations H, V and D; b) DIC strain maps indicate the equivalent Tresca strain; c) SEM images of the microstructure and the crack paths.

the elongation at fracture (ε_{max}) of 2.4% show a larger dispersion as these properties are more influenced by the natural presence of manufacturing defects [25,27,48]. Typical manufacturing-induced defects, such as lack of fusion or porosity, were identified from SEM images of fracture surfaces, Fig. 3.b-g.

The values of elastic modulus are summarised in Fig. 3.h where E vs temperature values are reported. The Al2618 + TiB_2 shows an elastic modulus of 85.2 GPa at room temperature, while it maintains a value of 78.7 GPa at 150 °C. At low temperatures, E was found to be equal to 88.1 GPa (−50 °C). Overall, the average increment compared to the base Al2618 forged alloy is approximately 13% [49]. The E data are well aligned with the linear fitting represented by a black dashed line, and the results can be particularly useful for thermo-mechanical simulation or for the design of components subjected to environments with extreme thermal variations (e.g. space).

Fracture toughness values obtained from the tests are reported in the plot in Fig. 4.a for the three orientations (H, V, D). The H orientation experienced the highest value of toughness having an average value of 23.9 MPa $\sqrt{m}$, while the V orientation showed an average value of 18.0 MPa $\sqrt{m}$ and the D orientation displayed a value of 15.3 MPa $\sqrt{m}$.

Exploiting the DIC analysis, the equivalent Tresca strain maps were obtained on the lateral surface (plane-stress loading condition) of the specimens, see Fig. 4.b. The maps are compared considering the frame on which the P_Q load is applied to the specimens (P_Q is the load used to compute the K_{IC} value [30]). The DIC maps highlight the strain accumulation at the crack tips for the three orientations: blue colour in the scale indicates the strain at yielding, $\varepsilon_y = 0.58\%$, and it is indicated on the scale bar with a red mark. The real crack path is represented with a black line over the strain maps, and SEM close-ups show the microstructure in the early region of the crack (Fig. 4.c). The melting pools typical of AM are clearly visible following chemical etching treatment and they are highlighted in yellow in the proximity of the crack.

The crack path analysis highlights the anisotropic behaviour of the material. In the V and D specimens, the crack preferentially propagates along melt pool boundaries (MPBs), which act as microstructurally favourable paths for crack growth. In contrast, in the H specimen the crack is forced to cross the melt pools, intersecting the MPBs rather than following them, leading to a higher resistance to crack propagation in the H orientation [50]. Furthermore, the higher resistance of the material to the crack advancement determines larger plastic deformation at the crack tip [51]. This is confirmed by the DIC analysis where the plastic region is significantly larger for the H orientation. Moreover, the plastic regions at the crack tip, visible on the strain maps, tend to differ depending on the printing orientation.

Regarding the comparison between the V and D orientations, the measured fracture toughness values show no significant variation between the two conditions. Qualitative inspection of the crack paths suggests that crack propagation in the D specimens is less tortuous than in the V specimens. This reduced crack deflection may facilitate crack advance and thereby contribute to the lower fracture toughness observed for the D orientation (Fig. 4.a).

See Fig. 5.a shows the fracture toughness values collected for Al2618 base and reinforced with TiB_2 (9 wt% similar to 7.1 wt% adopted in this study) in T6 treatment and manufactured by casting, forged Al2618 in T6 treatment with Circumferential-Longitudinal (CL) and Circumferential-Radial (CR) orientations, AM AlSi10Mg in the three orientations (V, D, H) in As Built (AB) and in T5 condition and AM Scalmalloy® in T5 treatment [27,51–54].

The K_{IC} values obtained in the present work (highlighted in red) are well in line with those of cast Al2618, both base and reinforced. On the other hand, it is recognized that forging can improve the static properties of aluminium alloys [55]; in fact, the toughness of Al2618 + TiB_2 is lower, as expected, than the values of forged Al2618. The trend of K_{IC} with the different printing orientations (higher performances for H,

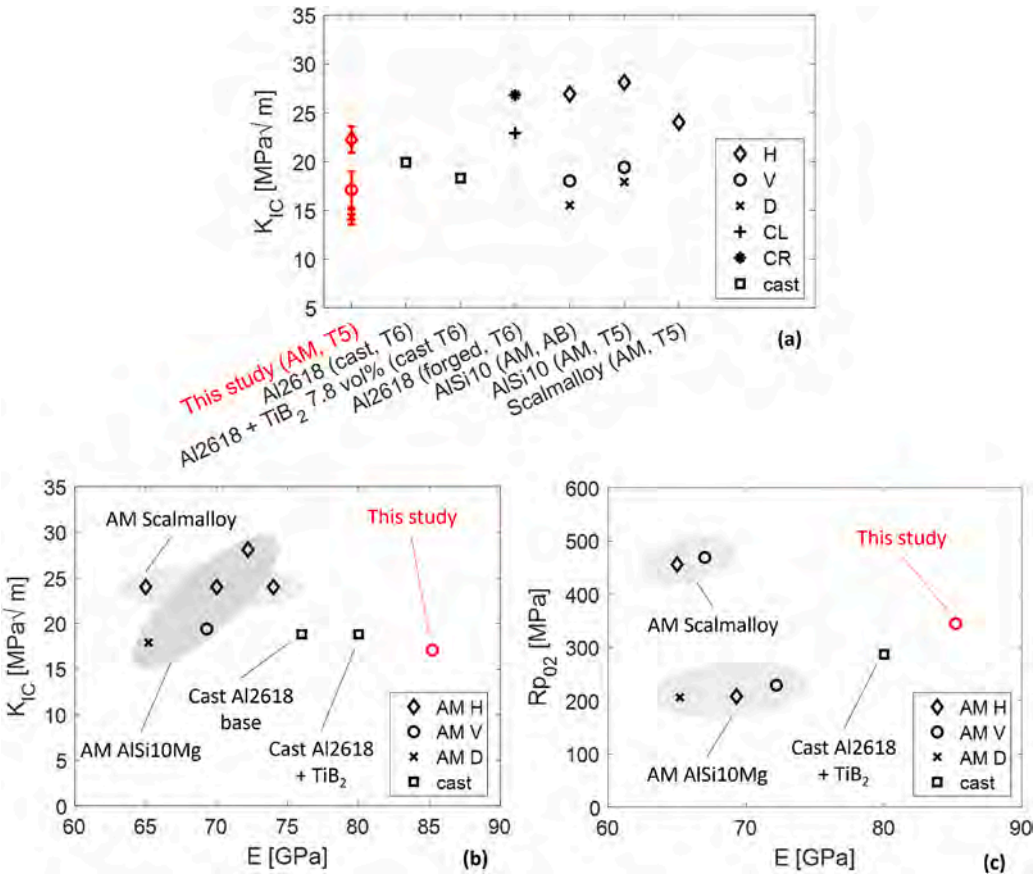

Fig. 5. a) Obtained K_{IC} for Al2618 + TiB_2 compared to literature data with different orientations and manufacturing methods [27,51–53]; b) K_{IC} vs E map for Al2618 + TiB_2, AlSi10Mg and Scalmalloy® with different orientation; c) Rp_{02} vs E map for Al2618 + TiB_2, AlSi10Mg and Scalmalloy® with different orientation [27,53,93,94].

lower for D and V orientation in the middle) is similar respect to AM AlSi10Mg data and AM Al2618 + TiB_2; this confirms the anisotropic behaviour which is determined by the AM-induced microstructure, as also confirmed in Fig. 4. The K_{IC} values for Scalmalloy® in V orientation remain of the same magnitude of the present MMC alloy.

In general, K_{IC} values for Al2618 + TiB_2 appear particularly promising, especially considering that the industrial adoption of MMCs is often hindered by their relatively low values of fracture toughness, which might be reduced by the presence of ceramic particles [56–58]. The principal factors contributing to this reduction include the microstructural barrier induced by the reinforcement particles on the plastic slip of the metallic matrix, as well as the presence of the particle clusters which reduce the local ligament. Other factors consider the particle fractures, particle–matrix debonding, and stress concentrations associated with irregular particle morphologies [53,59,60]. On this last point, the use of nearly spherical reinforcement particles could be beneficial in mitigating stress concentration and, consequently, in preserving higher K_{IC} [61].

In Fig. 5.b an Fig. 5.c, the static properties derived from tensile and fracture tests are compared with literature data using K_{IC} vs E and Rp_{02}

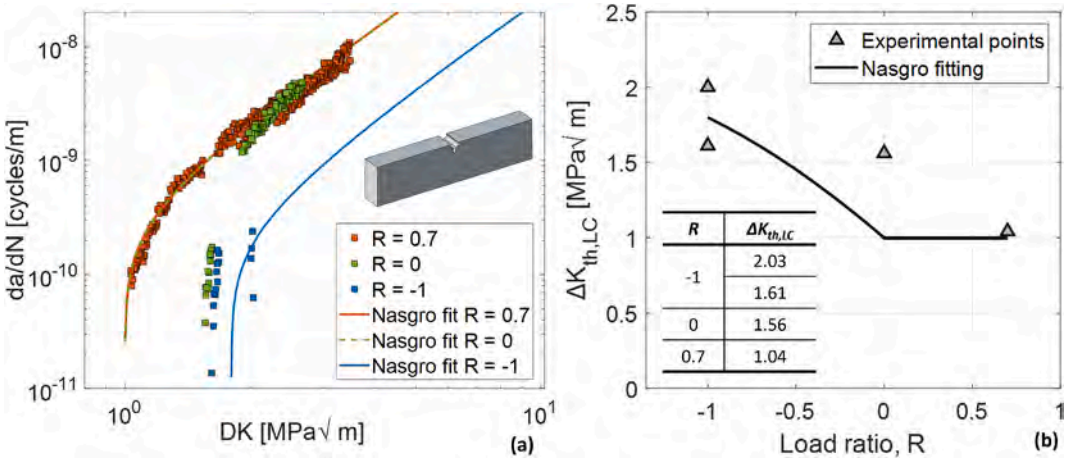

Fig. 6. a) Crack growth rate results on SEB specimens at different load ratios with Nasgro fitting; b) threshold values vs load ratio with Nasgro fitting.

Table 2
Nasgro fitting parameters (ΔK in MPa√m, crack length in m) [64].

C	m	*p*	*ΔK1*	*Cth+*	*Cth-*
5.28e-10	2.49	0.5	1	−0.1	0.15

vs *E* diagrams. It should be noted that the amount of available data in literature for generating a complete comparison of the mechanical properties is limited. AM Al2618 + TiB_2 data of vertical specimens (highlighted in red) are reported together with cast Al2618 + TiB_2, cast Al2618, AM AlSi10Mg and AM Scalmalloy® data. The higher elastic modulus of the AM Al2618 + TiB_2 emphasizes the potential adoption of the present alloy in stiffness-demanding applications without sacrificing fracture properties. A similar result is found for the Rp_{02} vs *E* diagram which shows that the higher elastic modulus makes the present MMC competitive with alloys characterized by higher values of Rp_{02}.

The interest in alloys with high elastic modulus is increasing, as materials with a high strength- and stiffness-to-weight ratio enable designers to minimize structural mass while maximizing the usable payload. In addition, higher values of elastic modulus reduce deformation, ensuring functional integrity and precise operation. Finally, materials with a high specific modulus increase natural frequencies, thereby lowering the risk of resonance phenomena that may lead to fatigue or catastrophic failure [16,62,63].

3.2. Fatigue properties

Results of FCG tests are summarized in Fig. 6.a in terms or crack growth rate vs applied ΔK; threshold values $\Delta K_{th,LC}$ resulting from the four CPLR tests are reported in Fig. 6.b for the three tested load ratios. The difference between the two $\Delta K_{th,LC}$ values at $R = -1$ can be mostly attributed to the presence of residual stresses in the SEB specimens, considering that they cannot be fully relieved by the T5 treatment. The complete Paris curve obtained at $R = 0.7$ is plotted with red datapoints and data obtained for $R = 0$ and $R = -1$ are plotted, respectively, in green and blue colours. The effect of high tensile RS is clear from the data on the Paris region at R = 0 which are completely overlapped with the R = 0.7 curve and thus they indicate that the effective load ratio is increased by the tensile RS. Therefore, a curve fitting option that allowed the crack opening function to be bypassed (α = 5.845, S_{max}/S_{flow} = 1.0) was used as suggested in the Nasgro user manual [64]. By using this option, the crack opening function *f* is zero for negative load ratios and equals R for positive load ratios (for all the details see [64]).

The curves in Fig. 6.a represent the Nasgro Equation (3) [64]:

$$\frac{da}{dN} = C\left[\left(\frac{1-f}{1-R}\right)\Delta K\right]^m \frac{\left(1-\frac{\Delta K_{th}}{\Delta K}\right)^p}{\left(1-\frac{K_{max}}{K_c}\right)^q} \tag{3}$$

the parameters C, m, p were obtained from the fitting of the FCG data, see Table 2. The parameter q was set to zero as the FCG data were limited to the stable crack propagation region. Table 2 also contains the Nasgro parameters for the threshold fitting shown in Fig. 6.b (ΔK1, Cth+, Cth-) [64].

The fitting curves for load ratios R = 0 and R = 0.7 are overlapped in Fig. 6.a (continuous red line and dashed green line), while the blue curve for R = −1 matches the threshold value at R = −1 (average value between the two repeated tests).

The crack propagation path and the local microstructure encountered by the crack tip were analysed for the specimen tested with the CPCA procedure at load ratio $R = 0$. A cut-up sample was extracted and analysed in the three regions along the crack path as highlighted (black rectangles indicated with a red arrow) in the schematic of Fig. 7. The cross-section under investigation corresponds to the central point of the crack front, i.e. plain strain condition.

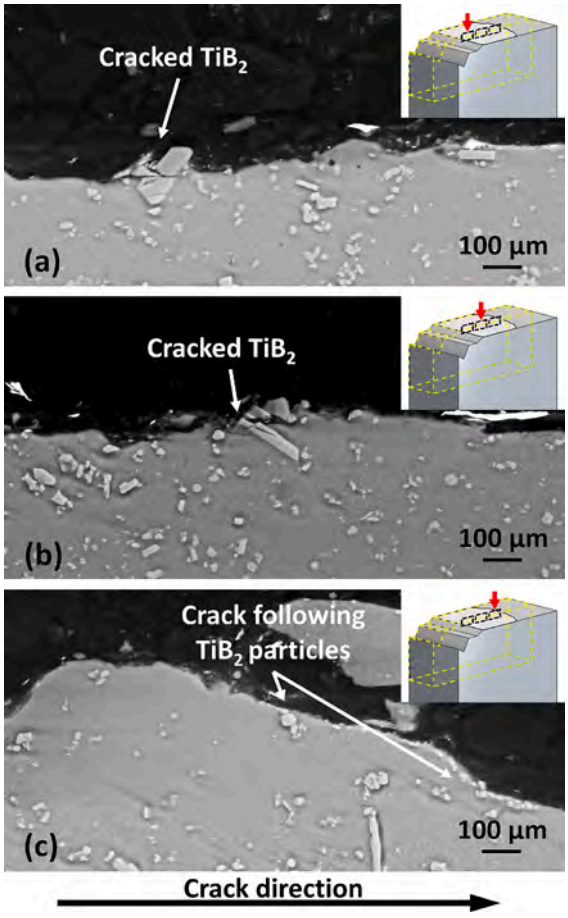

Fig. 7. a,b,c) SEM images of the sectioned crack path at different locations.

See Fig. 7.a and Fig. 7.b show the interaction of the crack with a large TiB_2 particle compared to the average dimension of the ex-situ reinforcement. It can be observed that the larger ceramic particles were fractured by the advancing crack front. This is in line with other literature findings which observed that ex-situ particles are more prone to crack compared to in-situ ones [65,66]. Plastic strain needed to fracture a particle has been observed to reduce with the increment of the particle size [67].

See Fig. 7.c highlights how the crack tends to propagate following the particles locations as it propagates in the particle–matrix interface [68]. This can be explained by the fact that high RS are concentrated at the interface between the particles and the matrix due to CTE mismatch [61]. Therefore, voids tend to form around the ceramic particles until they start to coalesce, thereby accelerating crack propagation. The propagation in the latter case can be described as driven by voids coalesce.

The fatigue data are presented in the SN diagram in Fig. 8.a in terms of stress range ($\Delta\sigma$) and number of cycles to failure N_f (the numerical results are contained in Appendix A). The estimated parameters of the SN fitting are reported in Table 3 [45]. Table 3 also contains the experimental fatigue limit ($\Delta\sigma_w$) and the number of cycles to failure at the knee-point of the SN diagram (N_{lim}).

The 95% bilateral scatter band was calculated using σ_{logN} and it is reported in Fig. 8.a. Failures, retested failures, and runouts are indicated using different symbols in the SN diagram in Fig. 8.a. A runout at stress range 190 MPa was observed and reported with a red dot, the same specimen was successively retested at 240 MPa experiencing a failure at almost $8 \bullet 10^6$ cycles (red square). This unexpected longer life at a high stress level compared to the fatigue limit was explained by analysing the fracture surface. For this specific specimen, the defect at the origin of the

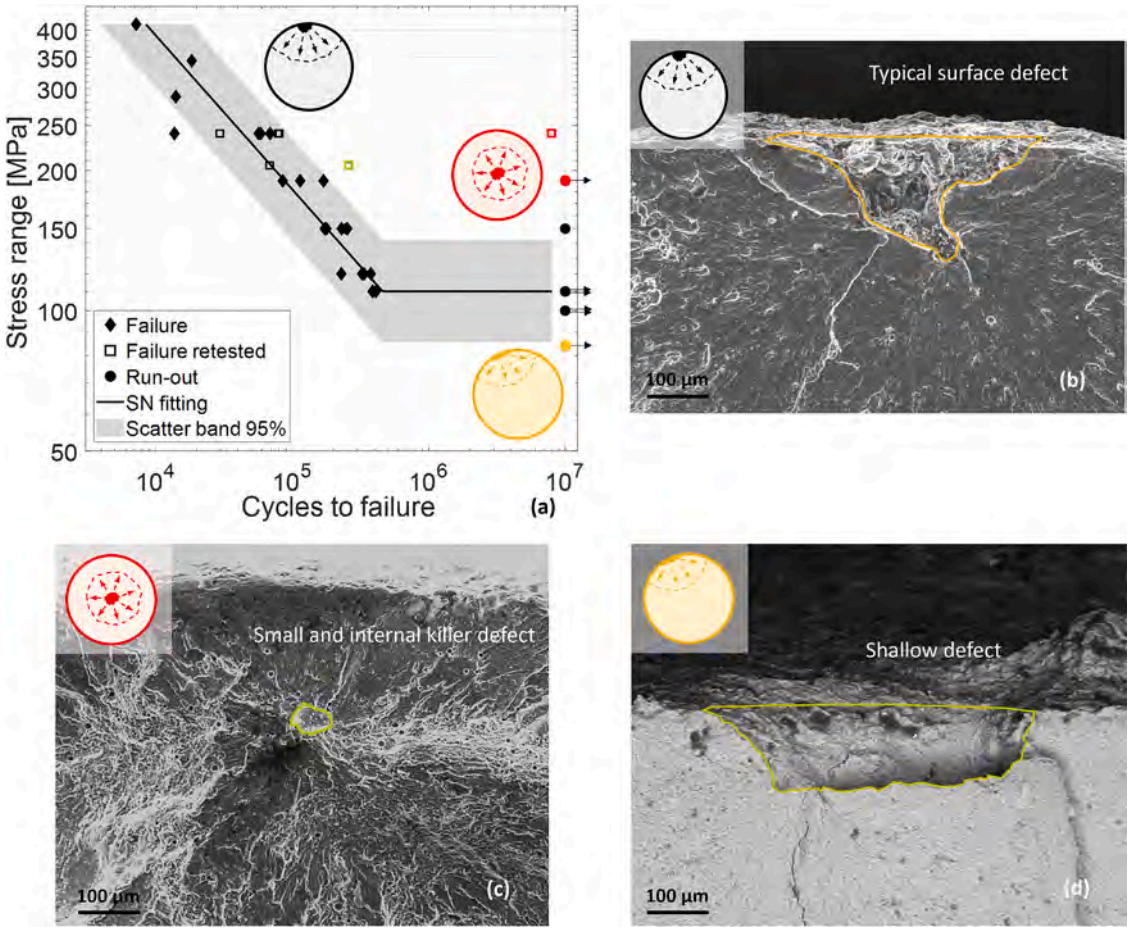

Fig. 8. a) SN diagram expressed in stress range of the specimen tested in AM Al2618 + TiB_2; b) SEM image of typical killer defect c) SEM image of internal killer defect; d) SEM image of shallow killer defect.

Table 3
Parameters of the SN fitting.

$\log_{10}(A)$	B	σ_{logN}	N_{lim} [cycles]	$\Delta\sigma_w$ [MPa]
11.835	−3.024	0.1692	459,889	110

failure was a small volumetric defect (a SEM image is reported in Fig. 8.c). For all the other specimens, the killer defects were detected on the specimen surfaces (SEM images of a typical surface killer defect is reported in Fig. 8.b). As a matter of fact, it is well known that most of the failures in fatigue of AM materials are triggered by surface or near-surface defects, which have a higher SIF for the same size and stress applied [35,69,70]. Moreover, specimens in which failure initiates from an internal defect have been demonstrated to generally yield a longer life [71–73].

A third type of failure was observed for the specimen displayed with the orange data which was characterized by a failure driven by a surface shallow defect (shown in Fig. 8.d). This test result will be analysed more in depth in the following considering also the measured in-depth RS.

The size of the defects at the origin of the failure were evaluated based on SEM fractographies. The defects sizes are expressed in terms of Murakami parameter $\sqrt{area}$ [74], and the average killer defect size was found to be 311 µm; all the values are reported in Fig. 9.a in a Gumbel probability plot.

From the fracture surfaces, the depths of the killer defects were also evaluated by measuring the maximum depth of the defects with respect to the external specimen surface, as schematized in Fig. 9.b. The average defect depth is 277 µm; the depths are fitted with a log-normal distribution shown in blue in Fig. 9.c (average and standard deviation are also reported). On the same plot, the measured RS in axial direction (0°) and circumferential direction (90°) of the fatigue specimens are also shown with the black colour. It should be noted that the in-depth RS values refer to a single specimen, however, their trend is aligned with stress profiles measured on similar AlSi10Mg sandblasted specimens [75]. The RS values measured on the surface (reported in red) refer to three different fatigue specimens and they demonstrate to be similar and consistent.

Considering the axial component of the RS, i.e. the component aligned with the load direction and thus having the greatest impact on fatigue life, the plot is divided in a compressive RS region (in green) and a tensile RS region (in red).

As expected, the sand blasting process induces superficial compressive RS. It can also be noticed that the tensile stresses are relatively high compared to the stress levels of the SN, in fact, they reach almost 300 MPa at 400 µm depth. Moreover, the plot shows that almost all the killer defects have the deepest point on the tensile RS region, thus experiencing a higher local load ratio with respect to the nominal $R = -1$. On the other hand, the shallow defect, as shown in Fig. 9.c, is completely embedded in the compressive RS region which granted the longer fatigue life compared to the specimens tested at the same stress range, as highlighted observing the orange data in Fig. 8.a.

Despite the large average defect size and the high tensile RS, the scatter of the fatigue data on the SN diagram remains limited in the 95% scatter band. Moreover, to complete the analysis and reinforce the previously described FCG results, the Paris curve fitting (Fig. 6.a) was employed in life predictions using the integration of the Nasgro model (the bypass option previously described in the Nasgro fitting was used).

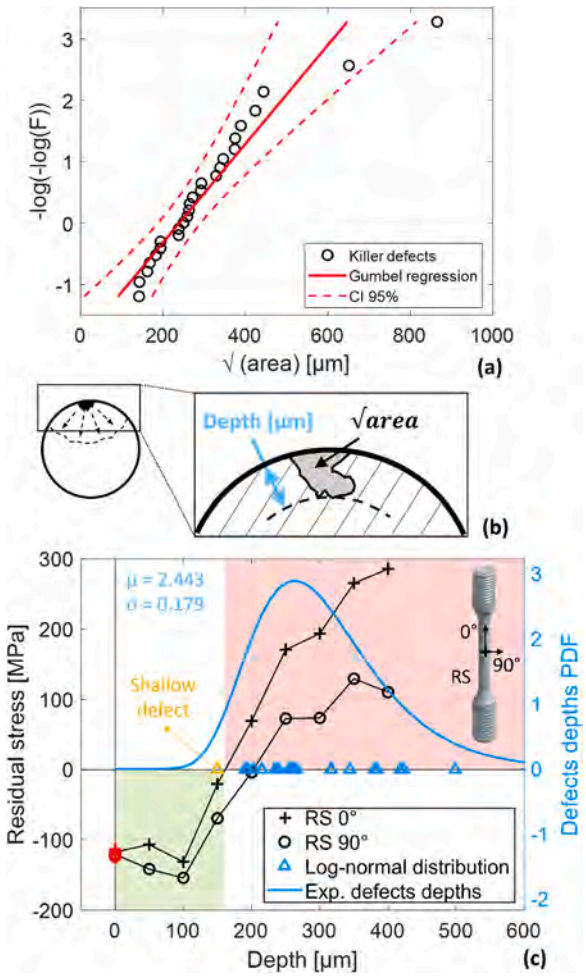

Fig. 9. a) killer defects Gumbel plot with fitting; b) schema of the considered killer defect depth c) overlapping of the defects' depths with the measured RS.

The effect of RS on the life was evaluated by introducing the axial (0°) RS profile shown in Fig. 9.c in the Nasgro SC35 crack model which allows to account for a univariant axisymmetric stress profile by means proper weight functions for the SIF solution [64]. The El Haddad parameter $\sqrt{area_0}$ was used in the Nasgro material model and it was obtained for the different stress ratios with the El Haddad formulation containing the theoretical endurance limit for defect-free material (estimated as $\Delta\sigma_{w,0} = 0.8 \bullet UTS$ for R = −1 and calculated with the Goodman line for R = 0 and R = −1), the obtained $\Delta K_{th,LC}$ from the CPLR tests and the crack shape factor $Y = 0.65$ for surface defects [76,77]. For the two load ratio under investigation, R = -1 and R = 0, $\sqrt{area_0}$ was found to be approximately the same as 48 μm.

Using the defined Nasgro model with RS implementation, the SN diagram was estimated by considering the 50% and 99% percentiles of the Gumbel defect distribution reported in Fig. 9.a, $\sqrt{area}_{50\%} = 311$ μm and $\sqrt{area}_{99\%} = 812$ μm, respectively. The 99% percentile represents the defect with a return period of 100 (the defect size that is exceeded once over 100 defects). In the analysis, given the $\sqrt{area}$ of the percentiles, the average aspect ratio (AR) of the killer defects which results in 1.74 was used to determine the crack depth a to be used in the Nasgro SC35 geometry definition (semi elliptical crack on a circular section): $a_{50\%} = 330$ μm and $a_{99\%} = 880$μm.

Fig. 10.a shows the estimated SN curves against the experimental data of the fatigue results. The predicted SN for the 50% percentile defect was obtained with and without the RS effect. It is clear how the SN without RS overpredicts the fatigue life, while the SN with the effect of RS properly models the experimental points. The SN for the 99% percentile defect represents the lower bound of the data points.

Fig. 10.b shows the comparison of experimental vs predicted life using Nasgro with and without accounting for RS. In the plot, together with the unitary line in black continuous line, the factor 2 error band is present with black dashed line. While the life predictions without RS are overestimating the experimental life with several points outside the error band, the model with RS shows a good accuracy, with all data lying within the error bounds. The effect of the compressive RS on the local load ratio is properly considered by the Nasgro model that predicts an almost exact life for the shallow defect (orange squared mark). This confirms the validity of the employed approach, the need of accounting RS in the predictions and the quality of the calibrated material model in performing life predictions at specimen level.

3.3. Defects analysis

Porosities were evaluated from XCT scans from the unfiltered volume data using the *Dragonfly* software. A triangular thresholding method was applied to the volume's histogram to segment the porosities [78]. Fig. 11.a1 shows the SEM image of a typical killer defect found on the fatigue specimens with a $\sqrt{area} = 318$ μm similar to the average killer defects size. The same defect is illustrated in Fig. 11.a2 identified from the XCT data by applying the porosity analysis.

For the fatigue life calculations, the projected area of the defects onto a plane perpendicular to the specimen axis was used to compute the

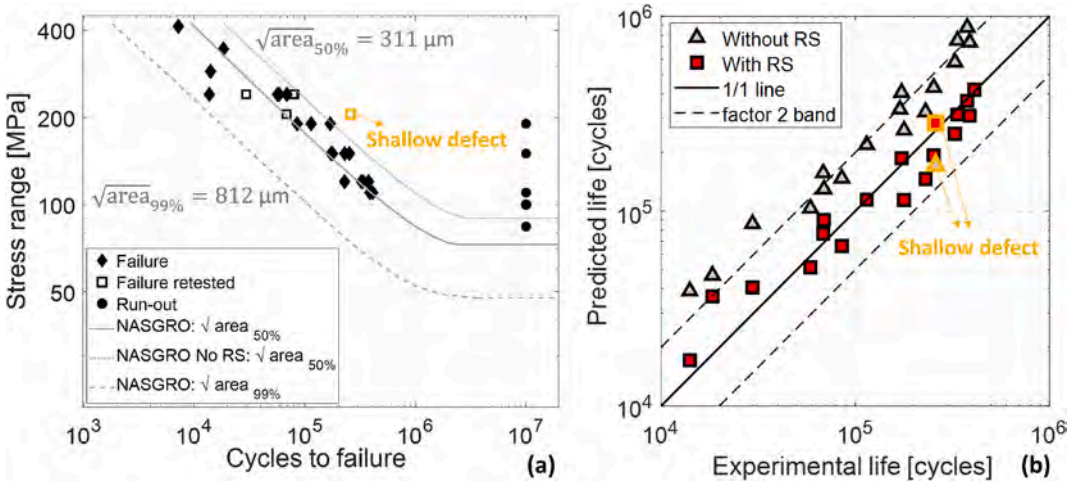

Fig. 10. a)SN prediction using Nasgro model on the 50% and 99% percentiles of the killer defects distribution; b) experimental vs predicted life for Nasgro model.

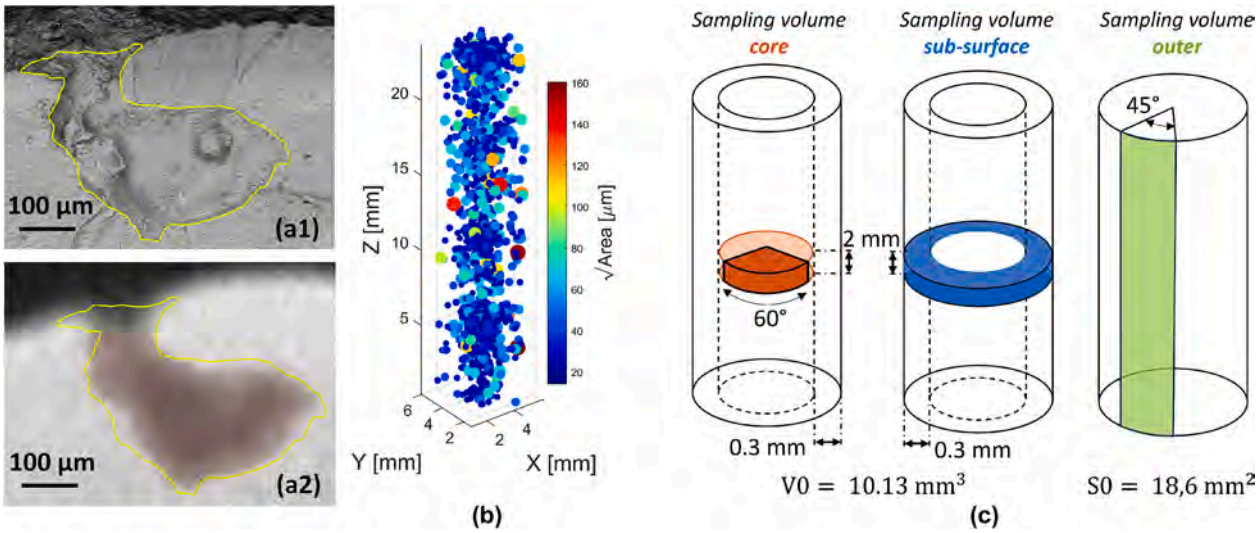

Fig. 11. a1, a2) same killer defect captured by SEM fracture image and XCT scan porosity analysis; b) typical porosity analysis resulted from the fatigue specimens XCT scans; c) block maxima sampling schemas for core, sub-surface and outer defects distributions.

Murakami parameter $\sqrt{area}$ [74]. An example showing the porosity results in terms of $\sqrt{area}$ and position of the defects is reported in Fig. 11.b.

From the porosity maps, the Block Maxima (BM) sampling was used to establish the maxima distribution of defect sizes [79]. A first division among all the flaws was adopted: volumetric defects, i.e. those defects that are not exposed to the atmosphere (*core* and *sub-surface* defects in Fig. 11.c), and surface defects (*outer* defects in Fig. 11.c), which are instead exposed to the atmosphere. While the porosity analysis is effective for volumetric defects, the outer defects are difficult to be automatically processed as they are exposed to the external air. The problem was addressed through the erode-dilate built-in tool of *Dragonfly* software, which was manually calibrated for each fatigue specimen [80].

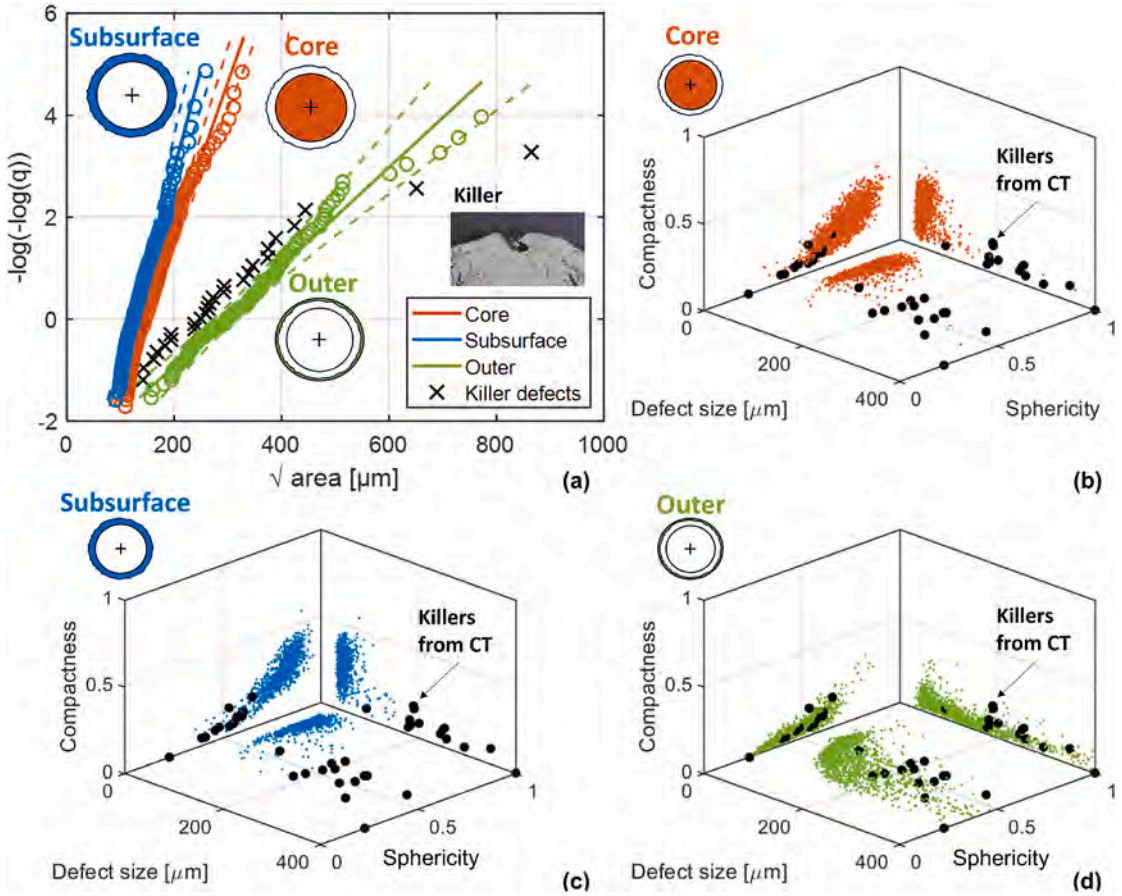

Fig. 12. a) Estimated maxima defects distributions for core (red), subsurface (blue) and outer (green) compared to killer defects (black); b,c,d) Compactness/Sphericity/Size diagrams for the core, subsurface and outer compared with the killer defects reconstructed from the XCT data.

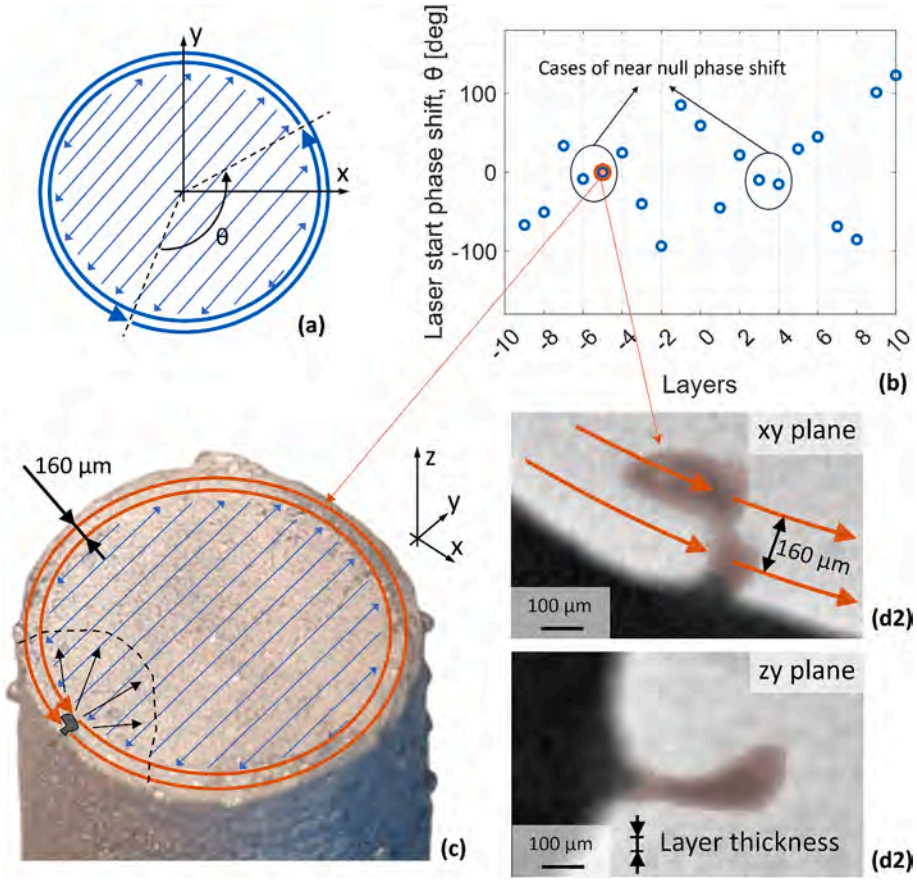

Fig. 13. a) laser path on the single layer and indication of the laser start phase shift θ; b) angle θ on a sample of 20 layers; c) killer defect formation on a layer with θ ≅ 0; d1, d2) typical killer defect compared with contour path and layer thickness dimensions.

The BM on outer defects was performed extracting the maximum out of a S_0 surface that was found dividing into eight angular sectors of 45° the external specimen surface, each sector is extending over the entire gauge length as shown in Fig. 11.c ($S_0 = 18.6$ mm^2).

As illustrated in Fig. 11.c, the volumetric defects were further subdivided into two volumes: the core region and the sub-surface region. The sub-surface region consists of an external shell with a thickness of 300 µm containing the defects that are in the contour region of the laser path and not exposed to the atmosphere. The core, instead, corresponds to the central cylinder of the specimens where the laser follows the hatching passages. These two different volumes were sectioned in the same sampling volume of $V_0 = 10.13$ mm^3. This value was chosen to guarantee a correct representation of the maxima distribution and to obtain enough maxima data for the Gumbel fitting.

Aiming to compare the three defect distributions (outer, sub-surface and core) with particular focus on the defect size, it is important to extrapolate each distribution with respect to a specific reference volume V^* or surface S^*. Starting from the maxima distribution obtained on BM volume V_0 or surface S_0, the distribution of the maximum defects on a different volume V^* or surface S^* can be obtained as:

$$F_{max|V^*,S^*} = \left[F_{max|V_0,S_0}\right]^n \tag{4}$$

F is the cumulative distribution function of the maxima and n is defined as $n = V^*/V_0$ for the core and sub-surface defects, while $n = S^*/S_0$ for the outer defects [79]. Equation (4) was applied to the core and sub-surface distributions to estimate the maxima defect distributions for the volume where killer defects were detected. This reference volume V^* corresponds to an external shell along the specimen gauge section with a thickness of 500 µm that is the maximum depth of the killer defects. For the outer defects Equation (5) was applied taking the reference surface S^*=*298.3* mm^2, which is the external surface of the specimen in the gauge region. The estimated statistical distributions for core, sub-surface and outer defects are reported on the Gumbel probability plot in Fig. 12. a together with the killer defects detected from fractography analysis (see also Fig. 9.a).

The volumetric defect distributions (core and sub-surface) are comparable with a slightly higher average defect for the core $\sqrt{area_{core}} =$ 164 µm compared to $\sqrt{area_{sub-surface}} = 140$ µm. On the other hand, the killer defects belong to a completely different population characterized by a larger average defect of $\sqrt{area_{killers}} = 311$ µm. This population is well captured by the maxima distribution of the outer defects (in green) which has an average defect size of $\sqrt{area_{outer}} = 389$ µm and the same slope.

To further analyse the differences between the three maxima distributions, Fig. 12.b-d show the defect size as $\sqrt{area}$ reported with compactness and sphericity parameters for all defects. Compactness and sphericity were selected as simple shape descriptors for the defects and are defined as:

$$Compactness = V_{defect}/V_{spherecircimscribed} \tag{5}$$

$$Sphericity = S_{sphereequivolume}/S_{defect} \tag{6}$$

V_{defect} is the volume of the defect, $V_{spherecircimscribed}$ is the volume of the sphere that is circumscribed to the defect, S_{defect} is the area of the external surface of the defect, $S_{sphereequivolume}$ the area of the external surface of the sphere having the same volume as the defect.

On the three-dimensional plots the black dots represent the reconstructed killer defects obtained on the porosity analysis of the XCT data. While for the core and sub-surface defects the killer population appears completely separated having lower sphericity and compactness, the

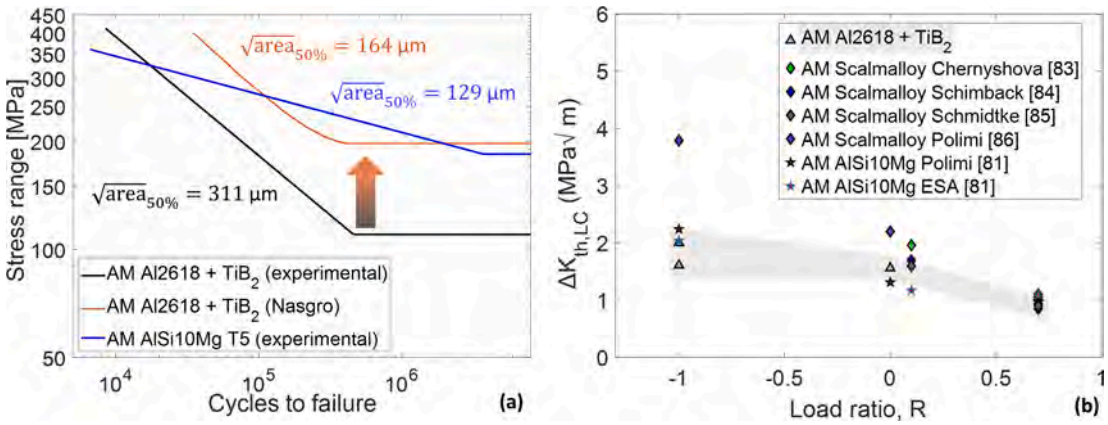

Fig. 14. a) SN diagram comparison with AlSi10Mg T5 and Nasgro estimation with the average size of core defects detected using the CT scan analysis; b) comparison of long crack thresholds $\Delta K_{th,LC}$ at different load ratios [81,83–86].

outer defect population perfectly matches the shape of the killer defects in the sphericity/compactness plane. This confirms that the performed BM sampling on the outer defects results in a good estimation of the critical defects distribution from XCT data and thus it can be used in fatigue life prediction.

The analysis of shape and size of the killer defects demonstrated that these defects are significantly larger than the volumetric and sub-surface counterparts, as discussed in Fig. 12.a. An hypothesis on the formation of such anomalies was formulated based on the analysis of the contour strategy and laser path during printing. The process parameters for the contour of this AM Al2618 + TiB_2 alloy were optimised based on the surface quality of the final parts, and a double contour laser passage was adopted. Each contour laser passage has a starting-ending point as shown in Fig. 13.a which is the point on the powder bed where the laser is switched on and it shuts down after the contour passage. The angular coordinates of the starting-ending points are randomly selected by the adopted slicing software. The relative angle between the starting-ending points of the internal contour passage and of the external contour passage is defined in Fig. 13.a as phase shift angle θ. This angle θ was extracted from the slicing file of the SLM machine in the printing layers nearby the killer defect location (± 10 layers along the height of the vertical specimens). It is observed that in several cases an almost zero phase shift was present in one or more layers as illustrated in the example of Fig. 13.b. This indicates the possible correlation between the superposition ($\theta = 0$) of the starting-ending points of the two contour passages with the formation of the killer flaw, as schematically represented in Fig. 13.c. The superposition can create a heat accumulation due to the longer time the laser remains in the same spot. This variation from the optimised energy density can affect the powder melting and the following solidification process. This hypothesis is strengthened by considering the typical shape and size of the killer defects. Fig. 13.d1 and Fig. 13.d2 show that the typical depth of the defects corresponds with the depth of the double contour passages; furthermore, the height of the defects is comparable with one or two layer thickness. These process-induced defects demonstrate that there is a significant margin of improvement in fatigue performances (by reducing the size and the number of flaws) of the studied AM Al2618 + TiB_2 printed with the selected process parameters.

3.4. Prospects for improving material performances

See Fig. 14.a shows the comparison between the SN diagram of the present AM Al2618 + TiB_2 (black line representing the fitted data) and the sandblasted AlSi10Mg T5 data (blue line) [81], both at load ratio $R = -1$. The AlSi10Mg data are here taken as a reference example of a consolidated aluminium alloy produced by PBF-LB. The comparison supports evaluating the detrimental effect of the critical flaws in fatigue properties and the fatigue limit for the studied AM Al2618 + TiB_2 [82]. The AlSi10Mg alloy displays fatigue lives up to one order of magnitude longer, this is mainly attributed to an average size of the killer defects of 129 µm in terms of $\sqrt{area}$, less than half of the present Al2618 + TiB_2 (311 µm). Assuming the average size of the core defects ($\sqrt{area_{core}} =$ 164 µm) as the critical defect in the present Al2618 + TiB_2, the corresponding SN diagram can be estimated considering the fitted NASGRO model described in Fig. 6 (the RS profile was considered in the SC35 crack geometry [64]). The resulting SN diagram (red line in Fig. 14.a) indicates the potential fatigue properties could reach those of the AlSi10Mg, especially in the short-life regime ($<10^5$ cycles) where the higher yield and ultimate tensile stresses provided by the TiB_2 reinforcement are particularly beneficial.

A final comparison is provided in Fig. 14.b considering the fatigue crack growth threshold $\Delta K_{th,LC}$ for different load ratios [81,83–86]. The present AM Al2618 + TiB_2 alloy is compared with different AM AlSi10Mg and AM Scalmalloy® datasets. The AM Al2618 + TiB_2 data are highlighted in the light grey region. For $R = 0.7$ and $R = 0$, $\Delta K_{th,LC}$ are comparable with the other alloys. On the other hand, at $R = -1$, the AM Al2618 + TiB_2 threshold is similar to the AlSi10Mg (as-built and T5 conditions), but lower than the Scalmalloy®. An important aspect to be considered in this comparison is that the crack growth threshold is strongly influenced by the presence of residual stresses. Fig. 9 shows the residual stress measurements for the fatigue specimens, which are particularly high towards the centre of the specimen. This observation remarks the fact that the potential relaxation of these detrimental tensile residual stresses could offer an additional margin of improvement for the fatigue performance of this alloy. The present study has evaluated the T5 condition which represents the thermal treatment optimised in a previous work of the authors for static properties [20], and that can be easily adoptable for large components. Other heat treatments, such as the T6 (solid solutioning step followed by an artificial ageing), could be investigated as thermal treatments at temperatures higher than the current T5 are beneficial for reducing the residual stresses and therefore improving the fatigue performances.

Another aspect that must be considered in the evaluation of the fatigue properties is the presence of a relatively high fraction of TiB_2 ceramic in the AM Al2618 + TiB_2 alloy that tends to influence the FCG properties. Wang et al found that fatigue cracks tend to propagate faster by increasing the TiB vol% in a MMC with Al A356 matrix and in T6 condition [68]. Moreover, the same result was obtained by other similar works in literature using different alloys [87–90]. Uniformity in ceramic particle distribution also plays an important role in reducing the fatigue crack growth rate [65].

A final remark concerns the potential adoption of the Al2618 + TiB_2 alloy for high-temperature applications. The elastic modulus values reported in Fig. 3 highlight the significant influence of TiB_2 reinforcement

on the alloy's static properties. Moreover, the Al2618 matrix itself exhibits promising mechanical behaviour at temperatures up to 200 °C [91,92]. Investigating the static and fatigue performance of the Al2618 + TiB_2 alloy under elevated-temperature conditions represents a promising direction for future research and applications.

4. Conclusions

This study presents a comprehensive static and fatigue characterization of Al2618-based MMC reinforced with in-situ and ex-situ TiB_2 particles. The paper demonstrates the promising mechanical performances of the AM Al2618 + TiB_2 alloy and its potential application in structural components. The main conclusions can be summarized as follows:

- The two steps powder production (in-situ and ex-situ methods) are effective in achieving a uniform TiB_2 particles dispersion in the final matrix of printed samples, also thanks to the solid adhesion of the μ-size ceramics to the Al2618 particles. The absence of particles clusters helps in reducing the manufacturing induced flaws which are detrimental for the mechanical properties.
- For the investigated vertical printing orientation, the yield stress is improved by 20% relative to the base Al2618, while the most significant improvement is achieved for the elastic modulus which increases by 13.2% compared to base Al2618, reaching up to + 30% respect to reference aluminium alloys for AM process (AlSi10Mg and Scalmalloy®); the high elastic modulus can be particularly useful in applications requiring high stiffness and can contribute to weight reduction and improved vibration control.
- The high ceramic reinforcement content does not significantly degrade fracture toughness, which remains only slightly lower than that of AlSi10Mg and Scalmalloy®.
- The crack propagation data were used to fit the Nasgro model which was then used to perform fatigue life predictions at specimen level. Precise fatigue life predictions were obtained thanks to the integration of the residual stresses profile in the model.
- XCT scan analysis revealed the presence of peculiar population of killer defects, likely originating from the contour laser path. The selection of the AM contour parameters is demonstrated to be crucial for this type of alloys, and it can influence the formation of detrimental defects. The predicted SN diagram considering the core average defect size highlights the potential competitive fatigue properties of the material with a refined contour parameters and thus a reduction of typical defects size; in fact, the predicted SN diagram shows values comparable to those of AlSi10Mg.
- Future developments should consider the thermal treatment, especially in relation to the relaxation of residual stresses: a T6 heat treatment which can release the residual stresses induced by the AM process can be a promising route for further investigations.

CRediT authorship contribution statement

Luca Mariotti: Writing – original draft, Investigation, Formal analysis, Data curation. **Giorgia Lupi:** Writing – review & editing, Formal analysis, Data curation. **Alessio Pozzoli:** Investigation, Formal analysis, Data curation. **Stefano Beretta:** Writing – review & editing, Methodology, Funding acquisition, Conceptualization. **Bartosz Madejski:** Investigation, Data curation. **Donato Girolamo:** Writing – review & editing, Supervision, Resources. **Riccardo Casati:** Writing – review & editing, Supervision, Project administration, Funding acquisition. **Luca Patriarca:** Writing – review & editing, Supervision, Methodology, Funding acquisition.

Declaration of competing interest

The authors declare that they have no known competing financial interests or personal relationships that could have appeared to influence the work reported in this paper.

Table 4
Results of fatigue testing.

Specimen ID	Δσ [MPa]	Load step	Test result	N_f [cycles]
ID1	100	1	Run Out	10,000,000
	240	2	Failure	78,990
ID2	240	1	Failure	68,931
ID3	110	1	Run Out	10,000,000
	240	2	Failure	80,524
ID4	110	1	Run Out	10,000,000
	240	2	Failure	29,566
ID5	240	1	Failure	58,744
ID6	412	1	Failure	7,206
ID7	344	1	Failure	18,392
ID8	288	1	Failure	14,059
ID9	240	1	Failure	56,766
ID10	120	1	Failure	229,103
ID11	120	1	Failure	335,797
ID12	120	1	Failure	376,940
ID13	150	1	Failure	178,252
ID14	150	1	Failure	173,078
ID15	190	1	Failure	169,726
ID16	100	1	Run Out	10,000,000
	205	2	Failure	68,430
ID17	110	1	Failure	387,932
ID18	110	1	Failure	410,177
ID19	120	1	Failure	325,707
ID20	240	1	Failure	13,734
ID21	190	1	Failure	114,455
ID22	150	1	Failure	230,078
ID23	190	1	Failure	85,302
ID24	84	1	Run Out	10,000,000
	200	2	Failure	259,121
ID25	190	1	Run Out	10,000,000
	240	2	Failure	7,927,877
ID26	150	1	Failure	253,299
ID27	150	1	Run Out	10,000,000
	240	2	Failure	76,046
ID28	150	1	Failure	244,765

Acknowledgements

This study was accomplished within the ENCOMPASS (Design of Enhanced Metal Matrix Composites for Additive Manufacturing of Space Structures) project funded by the European Space Agency Contract No. 4000139305/22/NL/AR.

Appendix A

See Table 4**.**

Appendix B. Supplementary data

Supplementary data to this article can be found online at https://doi.org/10.1016/j.ijfatigue.2026.109566.

Data availability

Data will be made available on request.

References

[1] DebRoy T, Wei HL, Zuback JS, Mukherjee T, Elmer JW, Milewski JO, et al. Additive manufacturing of metallic components – Process, structure and properties. Prog Mater Sci 2018;92:112–224. https://doi.org/10.1016/j.pmatsci.2017.10.001.
[2] Herzog D, Seyda V, Wycisk E, Emmelmann C. Additive manufacturing of metals. Acta Mater 2016;117:371–92. https://doi.org/10.1016/j.actamat.2016.07.019.
[3] Zhang D, Sun S, Qiu D, Gibson MA, Dargusch MS, Brandt M, et al. Metal Alloys for Fusion-Based Additive Manufacturing. Adv Eng Mater 2018;20. https://doi.org/10.1002/adem.201700952.

[4] Francois MM, Sun A, King WE, Henson NJ, Tourret D, Bronkhorst CA, et al. Modeling of additive manufacturing processes for metals: challenges and opportunities. Curr Opin Solid State Mater Sci 2017;21:198–206. https://doi.org/10.1016/j.cossms.2016.12.001.

[5] Raju R, Manikandan N, Palanisamy D, Arulkirubakaran D, Binoj JS, Thejasree P, et al. Review of Challenges and Opportunities in Additive Manufacturing, in 2022:: 23–9. https://doi.org/10.1007/978-981-19-0244-4_3.

[6] Babu SS, Love L, Dehoff R, Peter W, Watkins TR, Pannala S. Additive manufacturing of materials: Opportunities and challenges. MRS Bull 2015;40: 1154–61. https://doi.org/10.1557/mrs.2015.234.

[7] Bechir Chehab, Syam Unnikrishnan, Constellium Aheadd® CP1 alloy: Breakthrough productivity in PBF-LB Additive Manufacturing, (2022). https://www.metal-am.com/articles/constellium-aheadd-cp1-alloy-breakthrough-productivity-in-pbf-lb-3d-printing/ (accessed October 14, 2025).

[8] Chen Y, Zeng C, Ding H, Emanet S, Gradl PR, Ellis DL, et al. Thermophysical properties of additively manufactured (AM) GRCop-42 and GRCop-84. Mater Today Commun 2023;36. https://doi.org/10.1016/j.mtcomm.2023.106665.

[9] P.R. Gradl, C.S. Protz, D.L. Ellis, S.E. Greene, Progress in Additively Manufactured Copper-Alloy GRCop-84, GRCop-42, and Bimetallic Combustion Chambers for Liquid Rocket Engines, n.d.

[10] Li XP, Ji G, Chen Z, Addad A, Wu Y, Wang HW, et al. Selective laser melting of nano-TiB2 decorated AlSi10Mg alloy with high fracture strength and ductility. Acta Mater 2017;129:183–93. https://doi.org/10.1016/j.actamat.2017.02.062.

[11] T. Larimian, T. Borkar, Additive Manufacturing of In Situ Metal Matrix Composites, in: Additive Manufacturing of Emerging Materials, Springer International Publishing, Cham, 2019: pp. 1–28. Doi: 10.1007/978-3-319-91713-9_1.

[12] Essien U, Vaudreuil S. Issues in Metal Matrix Composites Fabricated by Laser Powder Bed Fusion Technique: a Review. Adv Eng Mater 2022;24. https://doi.org/10.1002/adem.202200055.

[13] Lijay KJ, Selvam JDR, Dinaharan I, Vijay SJ. Microstructure and mechanical properties characterization of AA6061/TiC aluminum matrix composites synthesized by in situ reaction of silicon carbide and potassium fluotitanate. Trans Nonferrous Met Soc Chin 2016;26:1791–800. https://doi.org/10.1016/S1003-6326(16)64255-3.

[14] Dadbakhsh S, Hao L. Effect of Al alloys on selective laser melting behaviour and microstructure of in situ formed particle reinforced composites. J Alloy Compd 2012;541:328–34. https://doi.org/10.1016/j.jallcom.2012.06.097.

[15] Dadbakhsh S, Hao L, Jerrard PGE, Zhang DZ. Experimental investigation on selective laser melting behaviour and processing windows of in situ reacted Al/Fe2O3 powder mixture. Powder Technol 2012;231:112–21. https://doi.org/10.1016/j.powtec.2012.07.061.

[16] Samal P, Vundavilli PR, Meher A, Mahapatra MM. Recent progress in aluminum metal matrix composites: a review on processing, mechanical and wear properties. J Manuf Process 2020;59:131–52. https://doi.org/10.1016/j.jmapro.2020.09.010.

[17] S.A.A. Alem, M.H. Sabzvand, P. Govahi, P. Poormehrabi, M. Hasanzadeh Azar, S. Salehi Siouki, R. Rashidi, S. Angizi, S. Bagherifard, Advancing the next generation of high-performance metal matrix composites through metal particle reinforcement, Advanced Composites and Hybrid Materials 2024 8:1 8 (2024) 1–68. Doi: 10.1007/S42114-024-01057-4.

[18] Parsons EM, Shaik SZ. Additive manufacturing of aluminum metal matrix composites: Mechanical alloying of composite powders and single track consolidation with laser powder bed fusion. Addit Manuf 2022;50. https://doi.org/10.1016/j.addma.2021.102450.

[19] Mussatto A, Ahad IU, Mousavian RT, Delaure Y, Brabazon D. Advanced production routes for metal matrix composites. Eng Rep 2021;3. https://doi.org/10.1002/eng2.12330.

[20] Lupi G, Mariotti L, Mistrini A, Larsson J, Patriarca L, Casati R. Microstructure and tensile properties of TIB2-reinforced Al-2618 thin walls produced by laser powder bed fusion. Mater Charact 2025;228:115372. https://doi.org/10.1016/j.matchar.2025.115372.

[21] Lupi G, Mariotti L, Lu S, Xu W, Patriarca L, Casati R. Unforeseen precipitation sequences in ex-situ/in-situ TiB2-reinforced Al2618 Composites Manufactured by Laser-based powder bed fusion. Mater Sci Eng A 2026;950:149500. https://doi.org/10.1016/j.msea.2025.149500.

[22] Martín A, Cepeda-Jiménez CM, Pérez-Prado MT. Gas atomization of γ-TiAl Alloy Powder for Additive Manufacturing. Adv Eng Mater 2020;22. https://doi.org/10.1002/adem.201900594.

[23] Lawley A. Atomization of Specialty Alloy Powders. JOM 1981;33:13–8. https://doi.org/10.1007/BF03354395.

[24] Bidulsky R, Gobber FS, Bidulska J, Ceroni M, Kvackaj T, Grande MA. Coated Metal Powders for Laser Powder Bed Fusion (L-PBF) Processing: a Review. Metals (Basel) 2021;11:1831. https://doi.org/10.3390/met11111831.

[25] Gorelik M. Additive manufacturing in the context of structural integrity. Int J Fatigue 2017;94:168–77. https://doi.org/10.1016/j.ijfatigue.2016.07.005.

[26] Sausto F, Romano S, Patriarca L, Miccoli S, Beretta S. Benchmark of a probabilistic fatigue software based on machined and as-built components manufactured in AlSi10Mg by L-PBF. Int J Fatigue 2022;165:107171. https://doi.org/10.1016/j.ijfatigue.2022.107171.

[27] Minerva G, Patriarca L, Foletti S, Beretta S. Static assessment of flawed thin AlSi10Mg parts produced by Laser Powder Bed Fusion. Mater Des 2022;224: 111292. https://doi.org/10.1016/j.matdes.2022.111292.

[28] IMR Metalle GmbH, (2025). https://www.imr-metalle.com/en/products/metal-powders.

[29] Treibacher industrie AG, (2025). https://treibacher.com/en/.

[30] E399 − 12. Standard Test Method for Linear-Elastic Plane-Strain Fracture Toughness KIc of Metallic Materials, (2012). internal-pdf://229.162.70.26/2012-Standard Test Method for Linear-Elastic P.pdf.

[31] American Society for Testing and Materials (ASTM), ASTM E647-11. Standard test method for measurement of fatigue crack growth rates, (2011).

[32] ASTM E739-91 Standard Practice for Statistical Analysis of Linear or Linearized Stress-Life (S-N) and Strain-Life (ε-N) Fatigue Data, Statistical Analysis of Fatigue Data (2009) 129-129–9.

[33] Test Methods for Tension Testing of Metallic Materials, (2004). Doi: 10.1520/E0008-04.

[34] Practice for Conducting Force Controlled Constant Amplitude Axial Fatigue Tests of Metallic Materials, (2021). Doi: 10.1520/E0466-21.

[35] Yadollahi A, Shamsaei N. Additive Manufacturing of Fatigue Resistant Materials: challenges and Opportunities. Int J Fatigue 2017;98:14–31. https://doi.org/10.1016/j.ijfatigue.2017.01.001.

[36] ECSS-Q-ST-70-80C(30July2021), (n.d.).

[37] Pippan R. THE GROWTH OF SHORT CRACKS UNDER CYCLIC COMPRESSION. Fatigue Fract Eng Mater Struct 1987;9:319–28. https://doi.org/10.1111/j.1460-2695.1987.tb00459.x.

[38] James MA, Forth SC, Newman JA. Load history effects resulting from compression precracking. J ASTM Int 2005;2:37–53. https://doi.org/10.1520/JAI12025.

[39] Zerbst U, Vormwald M, Pippan R, Gänser HP, Sarrazin-Baudoux C, Madia M. About the fatigue crack propagation threshold of metals as a design criterion - a review. Eng Fract Mech 2016;153:190–243. https://doi.org/10.1016/j.engfracmech.2015.12.002.

[40] Newman Jr JC, Yamada Y. Compression precracking methods to generate near-threshold fatigue-crack-growth-rate data. Int J Fatigue 2010;32:879–85. https://doi.org/10.1016/j.ijfatigue.2009.02.030.

[41] Newmanjr J, Schneider J, Daniel A, McKnight D. Compression pre-cracking to generate near threshold fatigue-crack-growth rates in two aluminum alloys. Int J Fatigue 2005;27:1432–40. https://doi.org/10.1016/j.ijfatigue.2005.07.006.

[42] Pourheidar A, Patriarca L, Madia M, Werner T, Beretta S. Progress in the measurement of the cyclic R-curve and its application to fatigue assessment. Eng Fract Mech 2022;260:108122. https://doi.org/10.1016/j.engfracmech.2021.108122.

[43] Maierhofer J, Kolitsch S, Pippan R, Gänser H-P, Madia M, Zerbst U. The cyclic R-curve – Determination, problems, limitations and application. Eng Fract Mech 2018;198:45–64. https://doi.org/10.1016/j.engfracmech.2017.09.032.

[44] Metallic materials-Fatigue testing-Statistical planning and analysis of data 122&23*,1**, 2003.

[45] A. International. E739-10 Standard Practice for Statistical Analysis of Linear or Linearized Stress-Life (S-N) and Strain-Life (ε-N). Fatigue Data 2015. https://doi.org/10.1520/E0739-10R15.

[46] W. Nelson, Maximum Likelihood Analysis of Multiply Censored Data, in: Applied Life Data Analysis, John Wiley & Sons, Inc., Hoboken, NJ, USA, 1982. Doi: 10.1002/0471725234.ch8.

[47] Perghem D, Salehnasab B, Beretta S, Shao S, Shamsaei N. ML-based detection of critical defects in additively manufactured parts via X-ray computed tomography. Mater Des 2025;260:115184. https://doi.org/10.1016/J.MATDES.2025.115184.

[48] Sausto F, Romano S, Patriarca L, Miccoli S, Beretta S. Benchmark of a probabilistic fatigue software based on machined and as-built components manufactured in AlSi10Mg by L-PBF. Int J Fatigue 2022;107171.

[49] John Gilbert Kaufman, Properties of aluminum alloys: Tensile, creep, and fatigue data at high and low temperatures, ASM International, 1999.

[50] Lupi G, de Menezes JTO, Belelli F, Bruzzo F, López E, Volpp J, et al. Fracture toughness of AlSi10Mg alloy produced by direct energy deposition with different crack plane orientations. Mater Today Commun 2023;37:107460. https://doi.org/10.1016/j.mtcomm.2023.107460.

[51] Lupi G, Minerva G, Patriarca L, Casati R, Beretta S. Fracture toughness of AlSi10Mg alloy produced by LPBF: effects of orientation and heat treatment. Int J Fract 2024; 247:329–44. https://doi.org/10.1007/s10704-024-00787-2.

[52] K. Anderson, J. Weritz, J.G. Kaufman, eds., Properties and Selection of Aluminum Alloys, ASM International, 2019. Doi: 10.31399/asm.hb.v02b.9781627082105.

[53] Wang F, Li J, Xu J, Li X, Zhang Y, Wang H. Investigation on fracture toughness of aluminum matrix composites reinforced with in situ titanium diboride particles. J Compos Mater 2012;46:2145–50. https://doi.org/10.1177/0021998311430158.

[54] Xiong ZH, Liu SL, Li SF, Shi Y, Yang YF, Misra RDK. Role of melt pool boundary condition in determining the mechanical properties of selective laser melting AlSi10Mg alloy. Mater Sci Eng A 2019;740–741:148–56. https://doi.org/10.1016/j.msea.2018.10.083.

[55] Manjunath GA, Shivakumar S, Fernandez R, Nikhil R, Sharath PC. A review on effect of multi-directional forging/multi-axial forging on mechanical and microstructural properties of aluminum alloy. Mater Today Proc 2021;47:2565–9. https://doi.org/10.1016/j.matpr.2021.05.056.

[56] Song M, Huang B. Effects of particle size on the fracture toughness of SiCp/Al alloy metal matrix composites. Mater Sci Eng A 2008;488:601–7. https://doi.org/10.1016/j.msea.2008.03.022.

[57] Pestes RH, Kamat SV, Hirth JP. Fracture toughness of Al4%Mg/Al2O3p composites. Mater Sci Eng A 1994;189:9–14. https://doi.org/10.1016/0921-5093(94)90396-4.

[58] Park BG, Crosky AG, Hellier AK. Fracture toughness of microsphere Al2O3–Al particulate metal matrix composites. Compos B Eng 2008;39:1270–9. https://doi.org/10.1016/j.compositesb.2008.01.005.

[59] Lewandowski JJ, Liu C, Hunt WH. Effects of matrix microstructure and particle distribution on fracture of an aluminum metal matrix composite. Mater Sci Eng A 1989;107:241–55. https://doi.org/10.1016/0921-5093(89)90392-4.

[60] S.-J. Hong, H.-M. Kim, D. Huh, C. Suryanarayana, B.S. Chun, Effect of clustering on the mechanical properties of SiC particulate-reinforced aluminum alloy 2024 metal matrix composites, Materials Science and Engineering: A 347 (2003) 198–204. Doi: 10.1016/S0921-5093(02)00593-2.
[61] Yi H, Ma N, Zhang Y, Li X, Wang H. Effective elastic moduli of Al–Si composites reinforced in situ with TiB2 particles. Scr Mater 2006;54:1093–7. https://doi.org/10.1016/j.scriptamat.2005.11.070.
[62] Amirkhanlou S, Ji S. A review on high stiffness aluminum-based composites and bimetallics. Crit Rev Solid State Mater Sci 2020;45:1–21. https://doi.org/10.1080/10408436.2018.1485550.
[63] Christudasjustus J, Larimian T, Esquivel J, Gupta S, Darwish AA, Borkar T, et al. Aluminum alloys with high elastic modulus. Mater Lett 2022;320:132292. https://doi.org/10.1016/j.matlet.2022.132292.
[64] Nasgro Fracture Mechanics and Fatigue Crack Growth Analysis Software Reference Manual, Version 9.2, 2020. www.nasgro.swri.org.
[65] Kumai S, Yoshida K, Higo Y, Nunomura S. Effects of the particle distribution on fatigue crack growth in particulate SiC/6061 aluminium alloy composites. Int J Fatigue 1992;14:105–12. https://doi.org/10.1016/0142-1123(92)90086-R.
[66] Sugimura Y, Suresh S. Effects of sic content on fatigue crack growth in Aluminum Alloys Reinforced with SiC Particles. Metall Trans A 1992;23:2231–42. https://doi.org/10.1007/BF02646016.
[67] Schwalbe K-H. On the influence of microstructure on crack propagation mechanisms and fracture toughness of metallic materials. Eng Fract Mech 1977;9:795–832. https://doi.org/10.1016/0013-7944(77)90004-2.
[68] Wang F, Meng X, Ma N, Xu J, Li X, Wang H. The relationship between TiB 2 volume fraction and fatigue crack growth behavior in the in situ TiB 2/A356 composites. J Mater Sci 2011;47:3361–6. https://doi.org/10.1007/s10853-011-6179-z.
[69] Andreau O, Pessard E, Koutiri I, Peyre P, Saintier N. Influence of the position and size of various deterministic defects on the high cycle fatigue resistance of a 316L steel manufactured by laser powder bed fusion. Int J Fatigue 2021;143. https://doi.org/10.1016/j.ijfatigue.2020.105930.
[70] Yukitaka M, Masahiro E. Quantitative evaluation of fatigue strength of metals containing various small defects or cracks. Eng Fract Mech 1983;17:1–15. https://doi.org/10.1016/0013-7944(83)90018-8.
[71] Syed AK, Vesga W, Dutton B, Berentshaw T, Zhang X. Defect tolerance and fatigue limit prediction for laser powder bed fusion Ti6Al4V. Int J Fatigue 2024;184. https://doi.org/10.1016/j.ijfatigue.2024.108285.
[72] Junet A, Messager A, Weck A, Nadot Y, Boulnat X, Buffiere JY. Internal fatigue crack propagation in a Ti-6Al-4V alloy: an in situ study. Int J Fatigue 2023;168. https://doi.org/10.1016/j.ijfatigue.2022.107450.
[73] Oguma H, Nakamura T. Fatigue crack propagation properties of Ti-6Al-4V in vacuum environments. Int J Fatigue 2013;50:89–93. https://doi.org/10.1016/j.ijfatigue.2012.02.012.
[74] Murakami Y. Inclusion Rating by Statistics of Extreme Values and its Application to Fatigue Strength Prediction and Quality Control of Materials. J Res Nat Inst Stand Technol 1994;99.
[75] F. Sausto, C. Tezzele, S. Beretta, Analysis of Fatigue Strength of L-PBF AlSi10Mg with Different Surface Post-Processes: Effect of Residual Stresses, Metals 2022, Vol. 12, Page 898 12 (2022) 898. Doi: 10.3390/MET12060898.
[76] Murakami Y. Material defects as the basis of fatigue design. Int J Fatigue 2012;41:2–10. https://doi.org/10.1016/j.ijfatigue.2011.12.001.
[77] N.E. Dowling, Mechanical Behavior of Materials: Engineering Methods for Deformation, Fracture, and Fatigue, 4th ed., Pearson, Harlow, 2013.
[78] Steinhilber F, Lachambre J, Coeurjolly D, Buffiere J-Y, Martin G, Dendievel R. A methodology for the 3D characterization of surfaces using X-ray computed tomography: Application to additively manufactured parts. Addit Manuf 2024;84:104144. https://doi.org/10.1016/j.addma.2024.104144.
[79] E.J. Gumbel, Statistics of Extremes, Columbia University Press, New York, 1957.
[80] *Dragonfly* user manual, https://www.theobjects.com/dragonfly/dfhelp/2024-1/Default.htm#Image%20Filtering/Morphology%20Filters.htm?Highlight=dilate, (2024).
[81] Sausto F, Tezzele C, Beretta S. Analysis of Fatigue Strength of L-PBF AlSi10Mg with Different Surface Post-Processes: effect of Residual Stresses. Metals (Basel) 2022;12:898. https://doi.org/10.3390/met12060898.
[82] H. Kitagawa, S. Takahashi, Applicability of fracture mechanics to very small cracks or the cracks in the early stage, in: Proc. 2nd Int. Conf. Mech. Behaviour of Materials - ICM2, 1976: pp. 627–631.
[83] Chernyshova P, Guraya T, Singamneni S, Zhu T, Chen ZW. Fatigue Crack Growth Behavior of Al-4.5Mg-0.6Sc-0.3Zr Alloy Processed by Laser Powder Bed Fusion. J Mater Eng Perform 2021;30:6743–51. https://doi.org/10.1007/S11665-021-05989-6/FIGURES/12.
[84] Schimbäck D, Mair P, Kaserer L, Perfler L, Palm F, Leichtfried G, et al. An improved process scan strategy to obtain high-performance fatigue properties for Scalmalloy®. Mater Des 2022;224:111410. https://doi.org/10.1016/J.MATDES.2022.111410.
[85] Schmidtke K. Qualification of SLM: additive manufacturing for aluminium. Technische Universität Hamburg 2020. https://doi.org/10.15480/882.2551.
[86] Perghem D, Rusnati L, Patriarca L, Uriati F, Beretta S. Comparison of Fatigue Life and Strength Models for Defective Materials: Application to Scalmalloy in Different Surface Conditions. Fatigue Fract Eng Mater Struct 2025;48:3185–205. https://doi.org/10.1111/ffe.14638.
[87] Vasudevan AK, Sadananda K. Fatigue crack growth in metal matrix composites. Scr Metall Mater 1993;28:837–42. https://doi.org/10.1016/0956-716X(93)90362-V.
[88] Kumai S, King JE, Knott JF. FATIGUE CRACK GROWTH BEHAVIOUR IN MOLTEN-METAL PROCESSED Sic PARTICLE-REINFORCED ALUMINIUM ALLOYS. Fatigue Fract Eng Mater Struct 1992;15:1–11. https://doi.org/10.1111/j.1460-2695.1992.tb00011.x.
[89] Chen ZZ, Tokaji K, Minagi A. Particle size dependence of fatigue crack propagation in SiC particulate-reinforced aluminium alloy composites. J Mater Sci 2001;36:4893–902. https://doi.org/10.1023/A:1011884103226.
[90] Botstein O, Arone R, Shpigler B. Fatigue crack growth mechanisms in AlSiC particulate metal matrix composites. Mater Sci Eng A 1990;128:15–22. https://doi.org/10.1016/0921-5093(90)90091-G.
[91] Leng Y, Porr WC, Gangloff RP. Tensile deformation of 2618 and AlFeSiV aluminum alloys at elevated temperatures. Scr Metall Mater 1990;24:2163–8. https://doi.org/10.1016/0956-716X(90)90504-A.
[92] Liu Y, Liu M, Luo L, Wang J, Liu C. The Solidification Behavior of AA2618 Aluminum Alloy and the Influence of Cooling Rate. Materials 2014;7:7875–90. https://doi.org/10.3390/ma7127875.
[93] Shakil SI, González-Rovira L, Cabrera-Correa L, de Dios López-Castro J, Castillo-Rodríguez M, Botana FJ, et al. Insights into laser powder bed fused Scalmalloy®: investigating the correlation between micromechanical and macroscale properties. J Mater Res Technol 2023;25:4409–24. https://doi.org/10.1016/j.jmrt.2023.06.228.
[94] Martucci A, Aversa A, Manfredi D, Bondioli F, Biamino S, Ugues D, et al. Low-Power Laser Powder Bed Fusion Processing of Scalmalloy®. Materials 2022;15:3123. https://doi.org/10.3390/ma15093123.